DOI: 10.1002/ ((please add manuscript number))
Article type: Full Paper

A Low-Bandgap Dimeric Porphyrin Molecule for 10% Efficiency Solar Cells with Small Photon Energy Loss

Liangang Xiao, Tianqi Lai, Xiang Liu, Feng Liu, Thomas P. Russell, Yi Liu, Fei Huang*, Xiaobin Peng* and Yong Cao*

L. G. Xiao, Dr. T. Q. Lai, X. Liu, Prof. F. Huang, Prof. X. B. Peng and Prof. Y. Cao
Institute of Polymer Optoelectronic Materials and Devices, State Key Laboratory of Luminescent Materials and Devices, South China University of Technology, 381 Wushan Road, Guangzhou 510640, China
Email: F.H: msfhuang@scut.edu.cn; X.P: chxbpeng@scut.edu.cn
Dr. Y. Liu
The Molecular Foundry, Lawrence Berkeley National Laboratory, Berkeley, California 94720, United State
E-mail: yliu@lbl.gov
Prof. F. Liu
Department of Physics and Astronomy, and Collaborative Innovation Center of IFSA (CICIFSA), Shanghai Jiaotong University, Shanghai 200240, P. R. China
Prof T. P. Russell
Materials Sciences Division, Lawrence Berkeley National Lab, Berkeley, California 94720, United States
Polymer Science and Engineering Department, University of Massachusetts, Amherst, Massachusetts 01003, United States

Keywords: dimeric porphyrin, organic solar cells, small photo energy loss, solvent vapor annealing

Abstract: Dimeric porphyrin molecules have demonstrated great potential as donor materials for high performance bulk heterojunction organic solar cells (OSCs). Recently reported dimeric porphyrins bridged by ethynylenes exhibited power conversion efficiencies more than 8%. In this study, we design and synthesize a new conjugated dimeric D-A porphyrin ZnP2BT-RH, in which the two porphyrin units are linked by an electron accepting benzothiadiazole (BT) unit. The introduction of BT unit enhances the electron delocalization, resulting in a lower highest occupied molecular orbital (HOMO) energy level and an increased molar extinction coefficient at the near-infrared (NIR) region. The bulk heterojunction solar cells with ZnP2BT-RH as the donor material exhibit a high power conversion efficiency up to 10% with a low energy loss (E_{loss}) of only 0.56 eV. The 10% PCE

is the highest for porphyrin-based OSCs with a conventional structure, and this E_{loss} is also the smallest among the small molecule-based OSCs with a PCE higher than 10% to date.

1. Introduction

In addition to the bulk heterojunction (BHJ) organic solar cells (OSCs) based on polymers,[1-8] those based on small molecules (SMs) have also attracted much attention due to advantages such as defined molecular structures, reproducible synthesis and less batch-to-batch variations in cell performance.[9-10] Furthermore, the shorter molecular lengths of SMs also result in lower entropic barriers and eliminate the chain entanglements,[11] thereby increasing the molecular packing and aggregation order in solid states, which can improve the inter-chain charge transportation. Therefore, power conversion efficiencies (PCEs) comparable to polymer solar cells have been reported for SM solar cells.[12-14]

The PCE of a solar cell is determined by its open circuit voltage (V_{OC}), short circuit current (J_{SC}) and fill factor (FF). In order to improve the J_{SC}, one of the strategies is to reduce the bandgap (E_g) of an active material to absorb more light in a broader spectrum range. However, the reduction of E_g is often accompanied by a decrease of V_{OC}. The energy loss (E_{loss}), defined as $E_{loss} = E_g - eV_{OC}$, is thus one of the important parameters to evaluate the performance of a solar cell.[15-17] The E_{loss} values of inorganic crystalline solar cells are usually about 0.34−0.48 eV and those of efficient perovskite solar cells are also less than 0.5 eV.[18-20] However, most OSCs suffer from high energy losses up to 0.7-0.8 eV, and the quantum efficiencies often drop dramatically at low E_{loss} values less than 0.6 eV.[21-24] Therefore, in order to achieve high PCEs, donor materials with low energy losses while retaining high J_{SC} values are highly desired.

Inspired by nature's photosynthesis which utilizes chlorophylls as strong chromophores, porphyrin analogues have been explored as the active materials for high performance organic solar cells with PCEs up to 9%.[25-40] Notably, some porphyrin-based OSCs show low energy

losses with high J_{SC} values. In order to further increase the J_{SC} values and therefore the PCEs of porphyrin-based OSCs, we developed a series of porphyrin dimers, in which porphyrin units are bridged by electron-rich ethynylene, diethynylene, diethynylenedithiophene or diethynylene-phenylene linkers, since extending the molecular conjugation length in oligoporphyrins was reported to be effective in increasing the molar coefficient and extending the absorption wavelength.[41-46] However, the highest PCE is only 8% for the dimeric porphyrin-based OSCs.[47-49]

Considering that alternating electron donor−acceptor (D-A) units in molecular structures can enhance the π electron delocalization and improve the light extinction coefficient due to intramolecular charge transfer,[50-54] herein, we incorporate an electron acceptor unit in between the two porphyrin units, and design and synthesize an A1-D-A2-D-A1 type dimeric porphyrin ZnP2BT-RH by appending 2-methylene-3-ethylrhodanine (RH) end units (A1) via ethynylene linkages to two porphyrin donor units (D) bridged by another electron acceptor unit (A2) benzothiadiazole (BT) (Scheme 1). ZnP2BT-RH shows an enhanced molar extinction coefficient of the NIR absorption peak than the previously reported porphyrin dimers without central electron-withdrawing unit. Furthermore, the electron-withdrawing BT unit can down-shift the highest occupied molecular orbital energy level (E_{HOMO}), thus increasing the gap between the E_{HOMO} of the donor and the lowest unoccupied molecular orbital energy level (E_{LUMO}) of $PC_{71}BM$. A high V_{OC} of 0.845 V, a J_{SC} of 17.66 mA cm^{-2}, a *FF* of 67.15% and a PCE up to 10.02% are achieved for the corresponding devices with a low energy loss (E_{loss}) of only 0.56 eV. The 10% PCE is the highest for porphyrin-based OSCs with a conventional structure, and this E_{loss} is also the smallest among the small molecule-based OSCs with a PCE higher than 10% to date.

2. Results and discussion

The synthetic route of the dimeric porphyrin small molecule ZnP2BT-RH is shown in Scheme 1 and Scheme S1. ZnP2BT-RH is a black solid with good thermal stability and good solubility in common organic solvents such as chloroform (CF), tetrahydrofuran (THF) and toluene, and its chemical structure was confirmed by NMR spectroscopy (Figure S1) and matrix-assisted laser desorption/ionization time-of light (MALDI-TOF) mass spectrometry (Figure S2). The ultraviolet-visible-near-infrared (UV-vis-NIR) absorption spectrum of ZnP2BT-RH in THF shows two absorption bands (Figure 1a) at 510 (Soret band) and 761 nm (Q band) with almost the same molar extinction coefficient (ε) of 2.24×10^5 M^{-1} cm^{-1} (Figure S3). Since the Soret band can be ascribed to the π–π* transition of the conjugated backbone and the Q band in the region of 700-850 nm is attributable to the intramolecular charge transfer (ICT) band,[55] the increased ε of the Q band indicates a more efficient ICT in ZnP2BT-RH than that in CS-DP (Scheme 1). [48]

Compared with the absorption spectrum in solution, that of ZnP2BT-RH film shows significantly red-shifted peaks with an onset at 885 nm, from which the optical band gap ($E_{g(opt)}$) is calculated to be 1.40 eV. In order to estimate the E_{HOMO} and E_{LUMO}, we measured the cyclic voltammetry (CV) of ZnP2BT-RH under an inert atmosphere in acetonitrile using tetrabutylammonium hexafluorophosphate (Bu_4NPF_6, 0.10 M) as the supporting electrolyte, a glassy carbon working electrode, a platinum wire counter electrode and an Ag/AgCl reference electrode. As shown in Table 1 and Figure S4, the onset oxidation potential (E_{ox}) of ZnP2BT-RH is 0.77 V *vs.* Fc/Fc^+, from which the E_{HOMO} is estimated to be −5.17 eV from $E_{HOMO} = -(Eox +4.4)$ eV, and the E_{LUMO} is -3.77 eV according to $E_{LUMO} = E_{HOMO} + E_{g(opt)}$. Compared with the E_{HOMO} (-4.96 eV) and E_{LUMO} (-3.74 eV) of CS-DP, the E_{HOMO} is notably reduced while the E_{LUMO} is quite similar.

To evaluate the photovoltaic performance of ZnP2BT-RH-based solar cells, solution-processed BHJ OSCs were fabricated using ZnP2BT-RH as the electron donor and [6,6]-phenyl C_{71}-butyric acid methyl ester ($PC_{71}BM$) as the electron acceptor with a conventional

device structure of ITO/PEDOT:PSS/active layer/PNDIT-F3N-Br/Al (ITO: indium tin oxide, PEDOT:PSS: poly(styrene sulfonate)-doped poly(ethylene-dioxythiophene), PNDIT-F3N-Br: poly[(9,9-bis(3'-((N,N-dimethyl)-N-ethylammonium)propyl)-2,7-fluorene)-alt-5,5'-bis(2,2'-thiophene)-2,6-naphthalene-1,4,5,8-tetracaboxylic-N,N'-di(2-ethylhexyl)imide]dibromide.[56] The current density (*J*)–voltage (*V*) curves of the ZnP2BT-RH-based OSCs are shown in Figure 2a and Figure S5-S6 with the photovoltaic parameters summarized in Table 2 and Table S1-S3. The donor-acceptor weight ratio was optimized to be 1:1.5, and the thickness of the active layer was ~115 nm. The solar cells based on as-cast ZnP2BT-RH/$PC_{71}BM$ films shows a PCE of 5.23% with a high *V*oc of 0.91 V. While thermal annealing (TA) treatment of the blend films at 135℃ only slightly improved the efficiency to 5.68%, further chloroform solvent vapor annealing (SVA) treatment (an overall TA+SVA treatment) dramatically enhanced the efficiency to 9.00% with a slightly reduced V_{OC} of 0.84 V but significantly increased J_{SC} and *FF* values to 16.49 mA cm^{-2} and 63.87%, respectively. Though the *FF* is smaller than that of CS-DP-based ones (69.80%), this PCE is higher than that of CS-DP-based ones (8.29%) thanks to the improved J_{SC} and V_{OC}, which could be ascribed to the deeper E_{HOMO} and enhanced ICT in ZnP2BT-RH due to the introduction of the electron withdrawing BT unit.

Surprisingly, different from the early reported OSCs based on monomeric porphyrins and other small molecules,[57-59] the performance of the devices under only SVA treatment is superior to those treated with TA + SVA. Upon chloroform SVA for 240 s, the PCE reaches 10.02% with a J_{SC} of 17.66 mA cm^{-2}, a V_{OC} of 0.845 V, and a *FF* of 67.15%. The 10% PCE is the highest for porphyrin-based OSCs with a conventional structure to date. Furthermore, the device performance is reproducible, and the efficiencies remain above 9% under different SVA times varying from 220 to 280 s. However, further TA after SVA treatment (SVA+TA) reduced the device performance significantly with a PCE, a J_{SC} and a FF of only 7.60%, 15.79 mA cm^{-2} and 55.97%, respectively. It is noted that the V_{OC} values still remain high in the

range of 0.84–0.91 V while the J_{SC} and *FF* values change dramatically under different processing conditions. From the optical bandgap and the V_{OC} values, the energy losses of the devices are calculated to be 0.49–0.56 eV. The E_{loss} of 0.56 eV is the smallest for small-molecule OSCs with PCE higher than 10% [12-14] and also one of the smallest for organic solar cells with PCE over 9% (Table S4).[1, 60-65] One of the reasons why the devices based on ZnP2BT-RH show such low energy losses can be the relatively high dielectric constant of ZnP2BT-RH (4.07 at 10 kHz) compared to that of previously reported porphyrin derivatives DPPEZnP-TEH (3.90 at 10 kHz) and those of other well-known OSC donors (Figure S7) because higher dielectric constant can facilitate charge separation and contribute to a lower energy loss.[23].

The external quantum efficiency (EQE) curves were measured to explore the spectral response of the devices fabricated with different post-treatments. As shown in Figure 2b, the devices can convert photons into electrons efficiently in the wavelength region of 300-800 nm, and lower EQEs tailing to 900 nm. While the as-cast devices show EQE peaks at 470 and 800 nm with high EQE values of 61% and 46%, respectively, TA treatment at 135℃ slightly increases the EQE values between 300 and 800 nm with a marginally blue-shifted photo response. The EQE peak in NIR region is at *ca.* 790 nm with an EQE of 50%. In line with the significantly enhanced J_{SC} values, the devices with the further SVA treatment (TA+SVA) show improved EQE values in the whole region from 300 to 900 nm, and the highest EQEs are observed for SVA-only devices with EQEs over 70% between 410 and 540 nm. Further TA treatment (SVA+TA) reduces the photo-to-electric response in the whole region compared with the SVA-only devices. Though the E_{LUMO} difference of ZnP2BT-RH and $PC_{71}BM$ (ΔE_{LUMO}) is smaller than the empirical threshold of 0.3 eV (energy level diagram was shown in Figure 1b), the high EQE values imply a low binding energy of the charge transfer excitons.

To investigate the molecular self-aggregation behaviors, the absorption spectra of the blend films upon different post-treatments are measured and shown in Figure 2c. While the NIR absorption peak of the as-cast blend film is at 788 nm, that of the TA treated ones is blue-shifted to 780 nm with a decreased intensity. On the contrary, SVA, TA+SVA and SVA+TA post-treatments red-shift the NIR peaks with enhanced absorption intensities. In addition, slight yet noticeable blue-shift can be observed for the SVA+TA samples compared to the absorption spectrum of SVA samples, which is similar to the absorption changes when the as-cast blend is thermally annealed, indicating the different aggregation behaviors induced by TA and SVA.

We measured the current density-voltage characteristics in the dark under reverse and forward biases (Figure S8) to investigate the rectification behaviors of the devices without any post-treatment and with SVA and SVA+TA treatments. Compared with the as-cast devices, the SVA treated ones show higher current density under forward bias but smaller dark current density under reverse bias, leading to an enhanced rectification ratio of 5.04×10^{5} versus 7.54×10^{4} for as-cast devices at ±2 V. Upon further TA treatment (SVA+TA), the forward current densities decrease while the reverse ones increase, reducing the diode performance. These results suggest that SVA treatment can suppress leakage current and improve the diode behavior but further TA has an adverse effect, possibly due to the overgrowth of ZnP2BT-RH crystalline phases and the vertical phase separation changes.[66]

We also investigated the hole mobilities of ZnP2BT-RH:$PC_{71}BM$ blend films under different processing conditions using the device structure of ITO/PEDOT:PSS/ZnP2BT-RH:$PC_{71}BM$/MoO_3/Ag by the SCLC (space-charge limited current) method. As shown in Figure S9 and listed in Table S5, the as-cast blend only shows a mobility of 1.21×10^{-5} cm^2 V^{-1} s^{-1}, and the TA treated blend shows a similar mobility of 1.43×10^{-5} cm^2 V^{-1} s^{-1}. However, the TA+SVA and SVA treated ZnP2BT-RH:$PC_{71}BM$ blend layers show mobilities up to 3.40×10^{-4} and 4.94×10^{-4} cm^2 V^{-1} s^{-1}, respectively, more than one order of magnitude higher

than these without SVA treatment. These values are also higher than that of CS-DP-based devices under TA+SVA treatments (1.44×10^{-4} cm^2 V^{-1} s^{-1}), indicating better charge transport in ZnP2BT-RH-based devices. In line with the FF changes, further TA treatment of the SVA-treated film (SVA+TA) reduced the hole mobility to 1.08×10^{-4} cm^2 V^{-1} s^{-1}.

To gain insight into exciton dissociation and charge generation of ZnP2BT-RH based solar cells under different processing conditions, we further investigated the relationships between the photocurrent density (J_{ph}) and the effective voltage (V_{eff}) of the cells (Figure 2d). J_{ph} and V_{eff} are defined by the equations of $J_{ph}=J_L-J_D$ and $V_{eff}=V_o-V_a$, where J_L and J_D are the current densities under illumination and in the dark, respectively, and V_o is the voltage at $J_{ph}=0$ and V_a is the applied voltage.[67] As shown in Figure 2d, J_{ph} values of the devices processed with TA+SVA and SVA are markedly higher and almost saturated (J_{sat}) at relatively lower V_{eff}, indicating more efficient exciton dissociation and carrier collection. On the other hand, J_{ph} values of the as-cast and TA treated devices are still not saturated even when V_{eff} is up to 5 V, an indication of severe charge combination. It is generally assumed that all the photo-generated excitons are dissociated into free charge carriers when the V_{eff} is high enough. Therefore, the saturation current (J_{sat}) only depends on the maximum exciton generation rate (G_{max}) calculated based on $J_{sat}=qLG_{max}$, where q is the elementary charge and L is the thickness of the active layer.[39, 68] The devices processed with SVA show a higher maximum exciton G_{max} of 1.05×10^{28} m^{-3} s^{-1} (J_{sat}=183.9 A m^{-2}) than that of the devices processed with TA+SVA (G_{max} is 1.01×10^{28} m^{-3} s^{-1} at a J_{sat} of 178.1 A m^{-2}). The increased G_{max} indicates the generation of more excitons, which is consistent with the enhanced absorbance as shown in Figure 2c. It should be noted that the small G_{max} difference cannot fully account for the big PCE difference. Another parameter, P(E,T), assessed by the J_{ph}/J_{sat} ratio under short circuit condition, should be taken into consideration to indicate the charge collection probabilities. The P(E,T) values for TA+SVA and SVA devices are 92.5% and 95.2%, respectively. The larger G_{max} and P(E,T) values for SVA devices correlate well with the higher J_{SC} and FF. For

SVA+TA devices, although the J_{sat} is similar to that of SVA devices, the moderate P(E,T) of 87.3% suggests inefficient charge separation, leading to a poor *FF* of 56.19% and a moderate PCE of 7.83%. All these results reveal that SVA processing is the most efficient to enhance the charge separation, which simultaneous improves J_{SC} and *FF*.

The recombination process of these devices was investigated by measuring the J_{SC} at various light intensities. In principle, J_{SC} shows a power-law dependence on light intensity for organic solar cells, which can be expressed as $J_{SC} \propto (P_{light})^S$ (P_{light} is the light intensity and S is the exponential factor).[69] When all free charges are swept out and collected at the electrodes prior to recombination, S value should be 1. Figure 3a shows J_{SC} against light intensity relationship of the devices under three different processing conditions, and the S values are calculated to be 0.931, 0.982 and 0.948 for the as-cast, SVA and SVA+TA devices, respectively. The highest S value of the SVA-treated device suggests the most effective suppression of bimolecular combination, leading to the highest J_{SC} and *FF*. V_{OC} values were also measured at various light intensities to get a deeper insight into the recombination mechanisms.[70] Figure 3b shows the relationships between the V_{OC} and the P_{light} of the devices under three different processing conditions. Generally, a slope of 1 K_BT/q implies that bimolecular recombination is the dominating mechanism (K_B is Boltzmann's constant, T is temperature and q is elementary charge), while a dependence of *V*oc on light intensity with a slope of 2 K_BT/q would be observed for trap-assisted or monomolecular recombination.[71-72] The slope of 1.20 K_BT/q for the ZnP2BT-RH-based devices without any post-treatment implies that the bimolecular recombination is dominant, possibly due to the good mixing of ZnP2BT-RH with $PC_{71}BM$, which provide sufficient interfaces for exciton separation but non-ideal crystallinity for efficient charge transport, leading to severe bimolecular recombination between the holes and electrons. On the other hand, the SVA and SVA+TA treated devices show slopes of 1.45 and 1.54 K_BT/q, respectively, suggesting that the

bimolecular recombination can be significantly suppressed by SVA treatment, commensurate with increased trap-assisted recombination in the devices.

We also investigated the morphology of ZnP2BT-RH:$PC_{71}BM$ active layers under different processing conditions, using atomic force microscopy (AFM), grazing incidence X-ray diffraction (GIXD) and resonant soft X-ray scattering (RSoXS). As shown in Figure S10, the root-means-square (RMS) roughness values of the as-cast and SVA treated films are less than 1 nm, and the TA+ SVA treated films show a slightly increased RMS of 1.5 nm. GIXD spectra of the pure ZnP2BT-RH films and blend films under different processing conditions can reveal more details of the intrinsic ordering structures of the components, as shown in Figure 4 and Figure S11. For the pure ZnP2BT-RH samples spuncast from pure THF solution, a sharp peak at 0.28 A^{-1} is observed in the low *q* region, attributable to lamellar stacking in the (100) crystalline direction. The crystalline nature of ZnP2BT-RH becomes less remarkable when pyridine was added as additive, as supported by the increased peak width, reduced peak intensity at 0.28 A^{-1} and the disappeared peaks at 0.57 A^{-1} (200) and 0.85 A^{-1} (300) from the out of plane GIXD pattern. For films treated with TA or SVA, higher order peaks at (200) and (300) reappeared, indicating that TA and SVA treatments promote the crystallization. Compared to the rest of the samples, the *d* spacing of the (100) peak of the SVA sample decreased slightly, in accordance with a tighter lamellar packing that is conducive to carrier transport. Furthermore, apparent π-π stacking peaks at 1.86 A^{-1} are observed after TA or SVA treatment. The similar crystallinity of TA, TA+SVA and SVA+TA treated samples is because the porphyrin crystallinity could be fixed after TA treatment and is hard to change even though with the following SVA treatment. Therefore, the apparent effect of TA treatment on crystallization is greater than that of SVA treatment. Subsequent TA treatment to SVA-treated film would endow crystallinity similar to TA-only film. For the blend samples, the as-cast films show a weak π-π stacking reflection peak in the in-plane direction, indicating a weak edge-on crystal orientation. A few diffusive Bragg rods are also observed in the in-plane

direction. These features could be ascribed to the self-assembly of ZnP2BT-RH molecules that form some thin layers in the donor domains.[48] The films under thermal annealing or solvent vapor annealing show quite broad (100) diffraction at 0.28 A^{-1} (2.24 nm) in all azimuthal angles, suggesting no preferred crystal orientation and the transformation of crystals from edge-on to face-on. In addition, a broad diffraction from $PC_{71}BM$ is seen at 1.31 A^{-1}. Importantly, for films treated with TA, TA+SVA, SVA or SVA+TA, obvious π–π stacking peak ascribable to ZnP2BT-RH can be seen at 1.86 A^{-1} (0.34 nm), which can correlate with the improved J_{SCs}. In addition, the peak areas of TA+SVA and SVA treated films were slightly larger than those of the TA and SVA+TA treated films, suggesting better crystallinity in TA+SVA and SVA treated films and are consistent with their better device performances.

The phase separation of these blend films was studied using resonant soft X-ray scattering (RSoXS) by taking advantage of the high optical contrast at the carbon K-edge photo energy of 284.2 eV. Shown in Figure 5 are the scattering profiles of the five blend films under different processing conditions. The as-cast films show very low scattering intensities and no obvious scattering peak, suggesting the lack of suitable phase separation. The inferior phase separation may be correlated with the good miscibility between the ZnP2BT-RH and $PC_{71}BM$ that is mediated by pyridine, similar to previously reported work that strong recombination is commonly observed in well-mixed systems.[27, 72] For the TA-treated blend film, a plateaued scattering peak appears at 0.022 A^{-1}, corresponding to a domain size of 28.6 nm. The low scattering intensity indicates a weak extent of phase separation, and thus, the devices based on thermally treated films display only slightly improved J_{SC} comparing to the as-cast films. Further SVA to the thermal annealing treated film leads to significantly enhanced scattering intensity in the whole q region, and an obvious peak is observed at 0.016 A^{-1}, corresponding to a distance of 39.2 nm. The significantly increased scattering intensity suggests the enhanced phase separation, which correlate well with the large improvement of

PCE from 5.68% to 9.00%. For the film treated with SVA only, the phase separated domain size (44.8 nm) is a little larger than that based on film treated with TA+SVA, which is beneficial for more balanced exciton separation and charge transportation. Furthermore, the SVA-only film also has better phase purity. These collective morphological features correlate well with the champion devices from solvent vapor annealing. However, for the film treated with SVA and further TA, a sharp upturn in the scattering in the very low q region is observed, which are consistent with the surface roughness and the device performances. Other factors like the diffusion of $PC_{71}BM$ to the layer of PEDOT:PSS and vertical phase separation change after further TA treatment, which are not observed in current characterization methods, may also contribute to the decrease of performance.

3. Conclusion

In summary, a dimeric porphyrin small molecule ZnP2BT-RH, in which the two porphyrin units are linked with an electron withdrawing unit BT, has been developed for OSCs. The introduction of BT unit can not only enhance the π electron delocalization to improve the intramolecular charge transfer and therefore the molar extinction coefficient at the NIR absorption band but also downshift the HOMO energy level, which are beneficial for the V_{OC} enhancement without sacrificing the J_{SC} values for ZnP2BT-RH–based OSCs. SVA treatment induces obvious π–π stacking and tightens lamellar packing, which would benefit for carrier transportation. Furthermore, suitable phase separation and improved phase purity of SVA-treated film greatly enhance exciton separation and carrier collection efficiency and reduce the recombination. After optimizing the processing conditions, excellent device performances with PCEs up to 10.02% are achieved with a low energy loss of only 0.56 eV, which is the smallest to date for small molecule-based OSCs with PCEs more than 10%. The 10% PCE is the highest for porphyrin-based BHJ solar cells and also ranks one of the highest for small molecule solar cells.

4. Experimental Section

Materials. All reagents were purchased from commercial sources (Aldrich, Acros, Energy chemical or Suna Tech Inc.) and used as received. Tetrahydrofuran (THF) triethylamine (Et_3N) and toluene were dried over Na/benzophenoneketyl and freshly distilled prior to use.

ZnP2BT-RH: Compound **1** (187mg, 0.10 mmol) was dissolved in THF (20 mL) and triethylamine (10 mL) with compound **2** (0.30 mmol). Then $Pd(PPh_3)_4$ (12 mg, 0.01mmol) and CuI (2 mg, 0.01mmol) were added. After the mixture was stirred at 60 ^oC for 48 h under argon, the reaction was quenched with saturated brine. After the mixture was extracted with chloroform, dried with anhydrous Na_2SO_4 and concentrated. The residue was column chromatographed on silica gel using CH_2Cl_2 as eluent to give a black solid of ZnP2BT-RH. (170 mg, 65% yield).

ZnP2BT-RH: ^{1}HNMR (500 MHz, $CDCl_3$) δ/ppm (ppm): ^{1}HNMR (500 MHz, $CDCl_3$) δ/ppm (ppm): 10.66-9.60 (m, 16H), 8.58-7.73 (m, 12H), 7.58 (s, 4H), 6.45(s, 2H), 4.36 (s, 12H), 3.64-3.27 (m, 8H), 2.45-2.15 (m, 4H), 2.15-1.04 (m, 86H), 0.91 (s, 6H). MALDI−TOF Mass (m/z): calculated for $C_{142}H_{150}N_{12}O_6S_{11}Zn_2$: 2601.73; found: 2602.25. UV-vis (THF), λ_{max}=508 nm.

Device Fabrication and Characterization: The methods and procedures in details were provided in Supporting Information.

Supporting Information

Supporting Information is available from the Wiley Online Library or from the author.

Acknowledgements

This work was financially supported by the grants from the National Natural Science Foundation of China (51773065 and 51473053), the National Key Research and Development Program of China (2017YFA0206602), International Science and Technology Cooperation Program of China (2013DFG52740), and the Fundamental Research Funds for the Central Universities. TPR were supported by the U.S. Office of Naval Research under contract N00014-15-1-2244**.** Portions of this research were carried out as a user project at the Molecular Foundry, and the X-ray experiments were carried out at beamline 7.3.3 and 11.0.1.2 at the Advanced Light Source, Lawrence Berkeley National Laboratory, all supported by the Office of Science, Office of Basic Energy Sciences, of the U. S. Department of Energy under Contract No. DE-AC02-05CH11231.

Received: ((will be filled in by the editorial staff))
Revised: ((will be filled in by the editorial staff))
Published online: ((will be filled in by the editorial staff))

References

[1] P. Cheng, M. Y. Zhang, T. K. Lau, Y. Wu, B. Y. Jia, J. Y. Wang, C. Q. Yan, M. Qin, X. H. Lu, X. W. Zhan, *Adv. Mater.* **2017**, *29*, 1605216-1605221.

[2] J. D. Chen, C. H. Cui, Y. Q. Li, L. Zhou, Q. D. Ou, C. Li, Y. F. Li, J. X. Tang, *Adv. Mater.* **2015**, *27*, 1035-1041.

[3] X. H. Ouyang, R. X. Peng, L. Ai, X. Y. Zhang, Z. Y. Ge, *Nat. Photonics* **2015**, *9*, 520-525.

[4] N. L. Qiu, H. J. Zhang, X. J. Wan, C. X. Li, X. Ke, H. R. Feng, B. Kan, H. T. Zhang, Q. Zhang, Y. Lu, Y. S. Chen, *Adv. Mater.* **2017**, *29*, 1604964-1604968.

[5] S. S. Li, L. Ye, W. C. Zhao, S. Q. Zhang, S. Mukherjee, H. Ade, J. H. Hou, *Adv. Mater.* **2016**, *28*, 9423-9429.

[6] Z. C. He, B. Xiao, F. Liu, H. B. Wu, Y. L. Yang, S. Xiao, C. Wang, T. P. Russell, Y. Cao, *Nat. Photonics* **2015**, *9*, 174-179.

[7] Y. H. Liu, J. B. Zhao, Z. K. Li, C. Mu, W. Ma, H. W. Hu, K. Jiang, H. R. Lin, H. Ade, H. Yan, *Nat. Commun.* **2014**, *5*, 5293-5300.

[8] W. C. Zhao, S. S. Li, H. F. Yao, S. Q. Zhang, Y. Zhang, B. Yang, J. H. Hou, *J. Am. Chem. Soc.* **2017**, *139*, 7148-7151.

[9] J. L. Wang, K. K. Liu, J. Yan, Z. Wu, F. Liu, F. Xiao, Z. F. Chang, H. B. Wu, Y. Cao, T. P. Russell, *J. Am. Chem. Soc.* **2016**, *138*, 7687-7697.

[10] L. G. Xiao, S. Chen, X. B. Chen, X. B. Peng, Y. Cao, X. J. Zhu, *J. Mater. Chem. C.* **2018**, *6*, 3341-3345.

[11] L. Zhang, F. Liu, Y. Diao, H. S. Marsh, N. S. Colella, A. Jayaraman, T. P. Russell, S. C. B. Mannsfeld, A. L. Briseno, *J. Am. Chem. Soc.* **2014**, *136*, 18120-18130.

[12] B. Kan, M. M. Li, Q. Zhang, F. Liu, X. J. Wan, Y. C. Wang, W. Ni, G. K. Long, X. Yang, H. R. Feng, Y. Zuo, M. T. Zhang, F. Huang, Y. Cao, T. P. Russell, Y. S. Chen, *J. Am. Chem. Soc.* **2015**, *137*, 3886-3893.

[13] D. Deng, Y. J. Zhang, J. Q. Zhang, Z. Y. Wang, L. Y. Zhu, J. Fang, B. Z. Xia, Z. Wang, K. Lu, W. Ma, Z. X. Wei, *Nat. Commun.* **2016**, *7*, 13740-13748.

[14] J. Wan, X. Xu, G. Zhang, Y. Li, K. Feng, Q. Peng, *Energ Environ. Sci.* **2017**, *10*, 1739-1745.

[15] R. A. J. Janssen, J. Nelson, *Adv. Mater.* **2013**, *25*, 1847-1858.

[16] D. Veldman, S. C. J. Meskers, R. A. J. Janssen, *Adv. Funct. Mater.* **2009**, *19*, 1939-1948.

[17] K. Gao, L. G. Xiao, Y. Y. Kan, B. L. Yang, J. B. Peng, Y. Cao, F. Liu, T. P. Russell, X. B. Peng, *J. Mater. Chem. C.* **2016**, *4*, 3843-3850.

[18] D. Q. Bi, C. Y. Yi, J. S. Luo, J. D. Decoppet, F. Zhang, S. M. Zakeeruddin, X. Li, A. Hagfeldt, M. Gratzel, *Nat. Energy* **2016**, *1*.

[19] P. K. Nayak, D. Cahen, *Adv. Mater.* **2014**, *26*, 1622-1628.

[20] M. Saliba, T. Matsui, K. Domanski, J. Y. Seo, A. Ummadisingu, S. M. Zakeeruddin, J.

P. Correa-Baena, W. R. Tress, A. Abate, A. Hagfeldt, M. Gratzel, *Science* **2016**, *354*, 206-209.

[21] W. W. Li, K. H. Hendriks, A. Furlan, M. M. Wienk, R. A. J. Janssen, *J. Am. Chem. Soc.* **2015**, *137*, 2231-2234.

[22] M. Wang, H. B. Wang, T. Yokoyama, X. F. Liu, Y. Huang, Y. Zhang, T. Q. Nguyen, S. Aramaki, G. C. Bazan, *J. Am. Chem. Soc.* **2014**, *136*, 12576-12579.

[23] K. Gao, L. S. Li, T. Q. Lai, L. G. Xiao, Y. Huang, F. Huang, J. B. Peng, Y. Cao, F. Liu, T. P. Russell, R. A. J. Janssen, X. B. Peng, *J. Am. Chem. Soc.* **2015**, *137*, 7282-7285.

[24] S. Chen, L. G. Xiao, X. J. Zhu, X. B. Peng, W. K. Wong, W. Y. Wong, *Chem. Commun.* **2015**, *51*, 14439-14442.

[25] L. G. Xiao, S. Chen, K. Gao, X. B. Peng, F. Liu, Y. Cao, W. Y. Wong, W. K. Wong, X. J. Zhu, *Acs. Appl. Mater. Inter.* **2016**, *8*, 30176-30183.

[26] H. M. Qin, L. S. Li, F. Q. Guo, S. J. Su, J. B. Peng, Y. Cao, X. B. Peng, *Energ Environ. Sci.* **2014**, *7*, 1397-1401.

[27] K. Gao, J. S. Miao, L. A. Xiao, W. Y. Deng, Y. Y. Kan, T. X. Liang, C. Wang, F. Huang, J. B. Peng, Y. Cao, F. Liu, T. P. Russell, H. B. Wu, X. B. Peng, *Adv. Mater.* **2016**, *28*, 4727-4733.

[28] T. X. Liang, L. A. Xiao, K. Gao, W. Z. Xu, X. B. Peng, Y. Cao, *Acs. Appl. Mater. Inter.* **2017**, *9*, 7131-7138.

[29] G. Moran, S. Arrechea, P. de la Cruz, V. Cuesta, S. Biswas, E. Palomares, G. D. Sharma, F. Langa, *J. Mater. Chem. A.* **2016**, *4*, 11009-11022.

[30] G. D. Sharma, L. Bucher, N. Desbois, E. Koukaras, C. H. Devillers, S. Biswas, C. P. Gros, *J. Mater. Chem. A.* **2018**, 6, 8449–8461.

[31] J. Kesters, P. Verstappen, M. Kelchtermans, L. Lutsen, D. Vanderzande, W. Maes, *Adv. Energy Mater.* **2015**, *5*, 1500218-1500237.

[32] C. Liu, L. Zhang, L. G. Xiao, X. B. Peng, Y. Cao, *Acs. Appl. Mater. Inter.* **2016**, *8*,

28225-28230.

[33] R. Mishra, R. Regar, R. Singhal, P. Panini, G. D. Sharma, J. Sankar, *J. Mater. Chem. A.* **2017**, *5*, 15529-15533.

[34] A. D. Zhang, C. Li, F. Yang, J. Q. Zhang, Z. H. Wang, Z. X. Wei, W. W. Li, *Angew. Chem. Int. Edit.* **2017**, *56*, 2694-2698.

[35] W. T. Hadmojo, D. Yim, H. Aqoma, D. Y. Ryu, T. J. Shin, H. W. Kim, E. Hwang, W. D. Jang, I. H. Jung, S. Y. Jang, *Chem. Sci.* **2017**, *8*, 5095-5100.

[36] H. D. Wang, L. G. Xiao, L. Yan, S. Chen, X. J. Zhu, X. B. Peng, X. Z. Wang, W. K. Wong, W. Y. Wong, *Chem. Sci.* **2016**, *7*, 4301-4307.

[37] V. Cuesta, M. Vartanian, P. de la Cruz, R. Singhal, G. D. Sharma, F. Langa, *J. Mater. Chem. A.* **2017**, *5*, 1057-1065.

[38] L. G. Xiao, T. X. Liang, K. Gao, T. Q. Lai, X. B. Chen, F. Liu, T. P. Russell, F. Huang, X. B. Peng, Y. Cao, *Acs. Appl. Mater. Inter.* **2017**, *9*, 29917-29923.

[39] L. G. Xiao, K. Gao, Y. D. Zhang, X. B. Chen, L. T. Hou, Y. Cao, X. B. Peng, *J. Mater. Chem. A.* **2016**, *4*, 5288-5293.

[40] L. G. Xiao, C. Liu, K. Gao, Y. J. Yan, J. B. Peng, Y. Cao, X. B. Peng, *Rsc. Adv.* **2015**, *5*, 92312-92317.

[41] G. D. Sharma, G. E. Zervaki, P. Angaridis, A. G. Coutsolelos, *Rsc. Adv.* **2014**, *4*, 50819-50827.

[42] Y. Matsuo, Y. Sato, T. Niinomi, I. Soga, H. Tanaka, E. Nakamura, *J. Am. Chem. Soc.* **2009**, *131*, 16048-16050.

[43] W. J. Park, S. H. Chae, J. Shin, D. H. Choi, S. J. Lee, *Synthetic Met.* **2015**, *205*, 206-211.

[44] J. L. Wang, Z. Wu, J. S. Miao, K. K. Liu, Z. F. Chang, R. B. Zhang, H. B. Wu, Y. Cao, *Chem. Mater.* **2015**, *27*, 4338-4348.

[45] X. F. Liu, Y. M. Sun, L. A. Perez, W. Wen, M. F. Toney, A. J. Heeger, G. C. Bazan, *J.*

Am. Chem. Soc. **2012**, *134*, 20609-20612.

[46] Q. Wu, D. Deng, K. Lu, Z.-X. Wei, *Chinese Chemical Letters* **2017**, *28*, 2065-2077.

[47] T. Lai, X. Chen, L. Xiao, L. Zhang, T. Liang, X. Peng, Y. Cao, *Chem. Commun.* **2017**, *53*, 5113-5116.

[48] S. Chen, L. Yan, L. Xiao, K. Gao, W. Tang, C. Wang, C. Zhu, X. Wang, F. Liu, X. Peng, W.-K. Wong, X. Zhu, *J. Mater. Chem. A.* **2017**, *5*, 25460-25468.

[49] T. Q. Lai, L. G. Xiao, K. Deng, T. X. Liang, X. B. Chen, X. B. Peng, Y. Cao, *Acs. Appl. Mater. Inter.* **2018**, *10*, 668-675.

[50] H. Burckstummer, E. V. Tulyakova, M. Deppisch, M. R. Lenze, N. M. Kronenberg, M. Gsanger, M. Stolte, K. Meerholz, F. Wurthner, *Angew. Chem. Int. Edit.* **2011**, *50*, 11628-11632.

[51] Y. Z. Lin, L. C. Ma, Y. F. Li, Y. Q. Liu, D. B. Zhu, X. W. Zhan, *Adv. Energy Mater.* **2013**, *3*, 1166-1170.

[52] J. L. Bredas, J. E. Norton, J. Cornil, V. Coropceanu, *Accounts Chem. Res.* **2009**, *42*, 1691-1699.

[53] L. G. Xiao, H. D. Wang, K. Gao, L. S. Li, C. Liu, X. B. Peng, W. Y. Wong, W. K. Wong, X. J. Zhu, *Chem-Asian J.* **2015**, *10*, 1513-1518.

[54] L. Yuan, K. Lu, B. Z. Xia, J. Q. Zhang, Z. Wang, Z. Y. Wang, D. Deng, J. Fang, L. Y. Zhu, Z. X. Wei, *Adv. Mater.* **2016**, *28*, 5980-5985.

[55] T. E. O. Screen, K. B. Lawton, G. S. Wilson, N. Dolney, R. Ispasoiu, T. Goodson, S. J. Martin, D. D. C. Bradley, H. L. Anderson, *J. Mater. Chem.* **2001**, *11*, 312-320.

[56] Z. H. Wu, C. Sun, S. Dong, X. F. Jiang, S. P. Wu, H. B. Wu, H. L. Yip, F. Huang, Y. Cao, *J. Am. Chem. Soc.* **2016**, *138*, 2004-2013.

[57] J. Min, X. C. Jiao, V. Sgobba, B. Kan, T. Heumuller, S. Rechberger, E. Spiecker, D. M. Guldi, X. J. Wan, Y. S. Chen, H. Ade, C. J. Brabec, *Nano Energy* **2016**, *28*, 241-249.

[58] K. Gao, W. Y. Deng, L. G. Xiao, Q. Hu, Y. Y. Kan, X. B. Chen, C. Wang, F. Huang, J.

B. Peng, H. B. Wu, X. B. Peng, Y. Cao, T. P. Russelle, F. Liu, *Nano Energy* **2016**, *30*, 639-648.

[59] B. Kan, Q. Zhang, M. M. Li, X. J. Wan, W. Ni, G. K. Long, Y. C. Wang, X. Yang, H. R. Feng, Y. S. Chen, *J. Am. Chem. Soc.* **2014**, *136*, 15529-15532.

[60] K. Kawashima, Y. Tamai, H. Ohkita, I. Osaka, K. Takimiya, *Nat. Commun.* **2015**, *6*, 10085-10093.

[61] H. J. Bin, Z. G. Zhang, L. Gao, S. S. Chen, L. Zhong, L. W. Xue, C. Yang, Y. F. Li, *J. Am. Chem. Soc.* **2016**, *138*, 4657-4664.

[62] J. Liu, S. S. Chen, D. P. Qian, B. Gautam, G. F. Yang, J. B. Zhao, J. Bergqvist, F. L. Zhang, W. Ma, H. Ade, O. Inganas, K. Gundogdu, F. Gao, H. Yan, *Nat. Energy* **2016**, *1*, 16089-16095.

[63] J. Zhang, K. Jiang, G. Yang, T. Ma, J. Liu, Z. Li, J. Y. L. Lai, W. Ma, H. Yan, *Adv. Energy Mater.* **2017**, 1602119-1602126.

[64] Z. Du, X. Bao, Y. Li, D. Liu, J. Wang, C. Yang, R. Wimmer, L. W. Städe, R. Yang, D. Yu, *Adv. Energy Mater.*, 1701471-1701482.

[65] D. Baran, T. Kirchartz, S. Wheeler, S. Dimitrov, M. Abdelsamie, J. Gorman, R. S. Ashraf, S. Holliday, A. Wadsworth, N. Gasparini, P. Kaienburg, H. Yan, A. Amassian, C. J. Brabec, J. R. Durrant, I. McCulloch, *Energ Environ. Sci.* **2016**, *9*, 3783-3793.

[66] K. Sun, Z. Y. Xiao, S. R. Lu, W. Zajaczkowski, W. Pisula, E. Hanssen, J. M. White, R. M. Williamson, J. Subbiah, J. Y. Ouyang, A. B. Holmes, W. W. H. Wong, D. J. Jones, *Nat. Commun.* **2015**, *6*, 6013-6021.

[67] P. W. M. Blom, V. D. Mihailetchi, L. J. A. Koster, D. E. Markov, *Adv. Mater.* **2007**, *19*, 1551-1566.

[68] J. L. Wu, F. C. Chen, Y. S. Hsiao, F. C. Chien, P. L. Chen, C. H. Kuo, M. H. Huang, C. S. Hsu, *Acs. Nano.* **2011**, *5*, 959-967.

[69] S. R. Cowan, A. Roy, A. J. Heeger, *Phys. Rev. B.* **2010**, *82*, 245207-245216.

[70] W. L. Leong, S. R. Cowan, A. J. Heeger, *Adv. Energy Mater.* **2011**, *1*, 517-522.

[71] L. J. A. Koster, V. D. Mihailetchi, R. Ramaker, P. W. M. Blom, *Appl. Phys. Lett.* **2005**, *86*, 123509-123511.

[72] M. M. Mandoc, W. Veurman, L. J. A. Koster, B. de Boer, P. W. M. Blom, *Adv. Funct. Mater.* **2007**, *17*, 2167-2173.

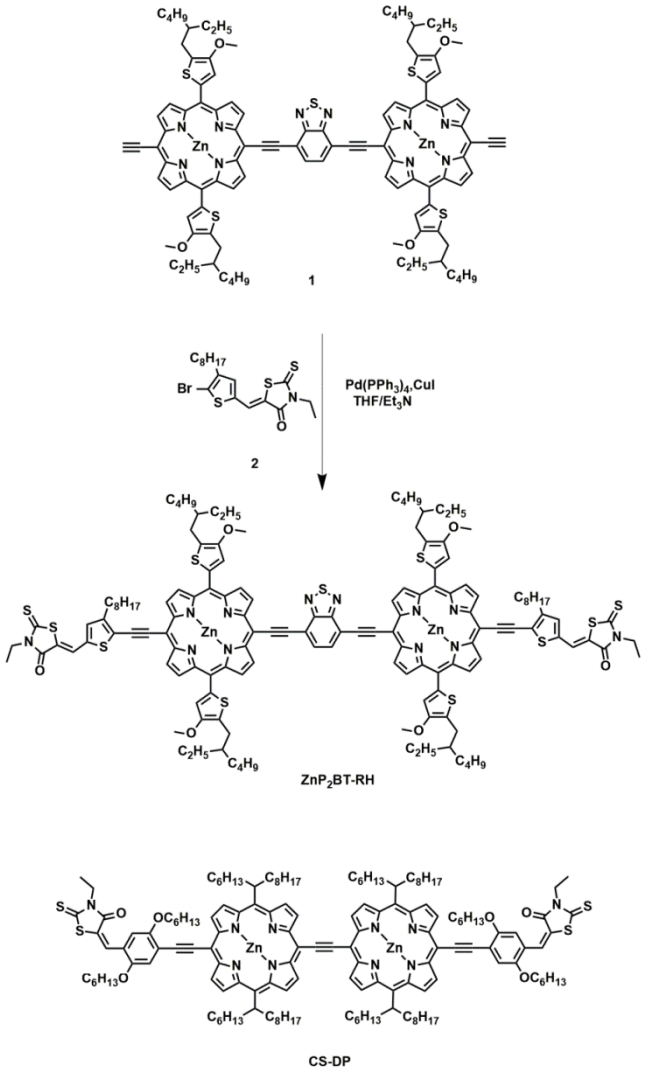

Scheme 1. The synthetic route of ZnP2BT-RH and chemical structure of CS-DP.

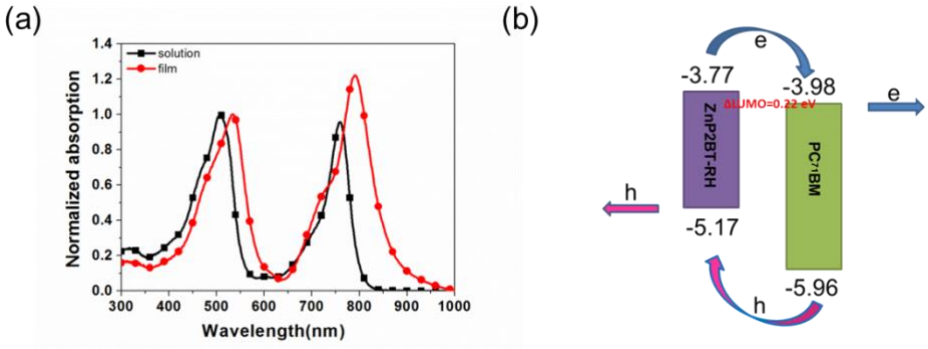

Figure 1. a) Normalized UV–vis–NIR absorption spectra of ZnP2BT-RH in solution (THF) and in film; b) the energy level diagram of ZnP2BT-RH and $PC_{71}BM$.

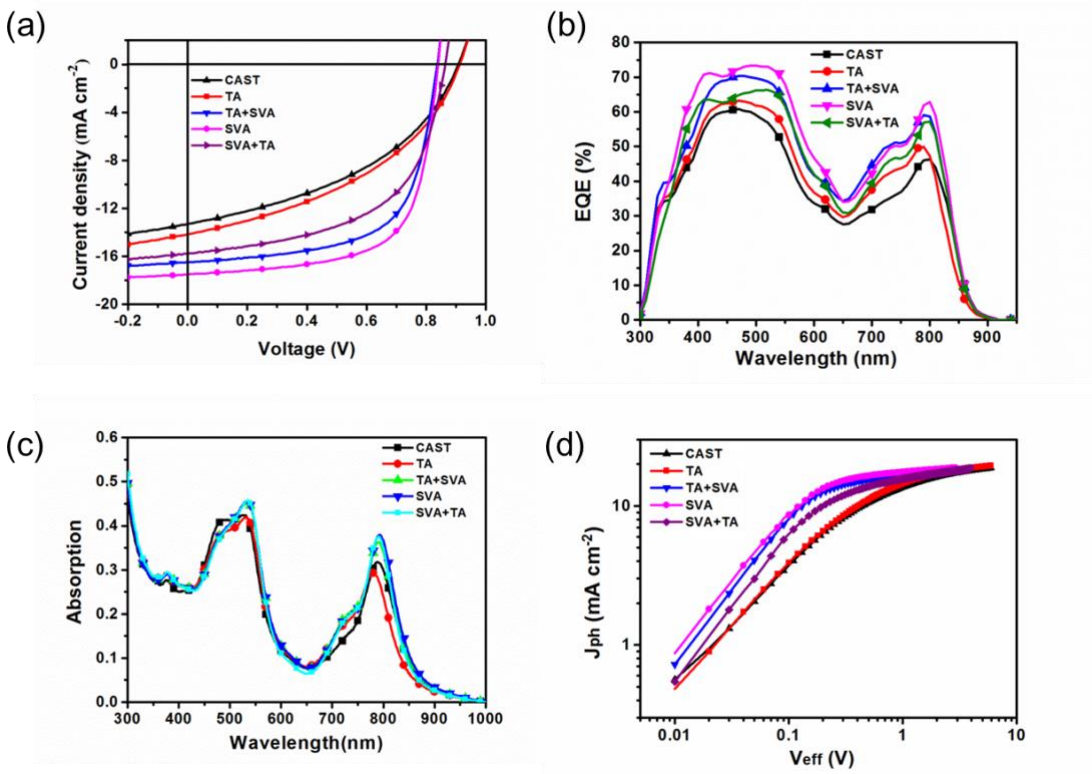

Figure 2. a) *J-V* curves, b) EQE curves of ZnP2BT-RH-based solar cells, c) the absorption spectra of ZnP2BT-RH/ $PC_{71}BM$ blend films, and d) photocurrent density versus effective voltage curves of the ZnP2BT-RH based solar cells under different processing conditions.

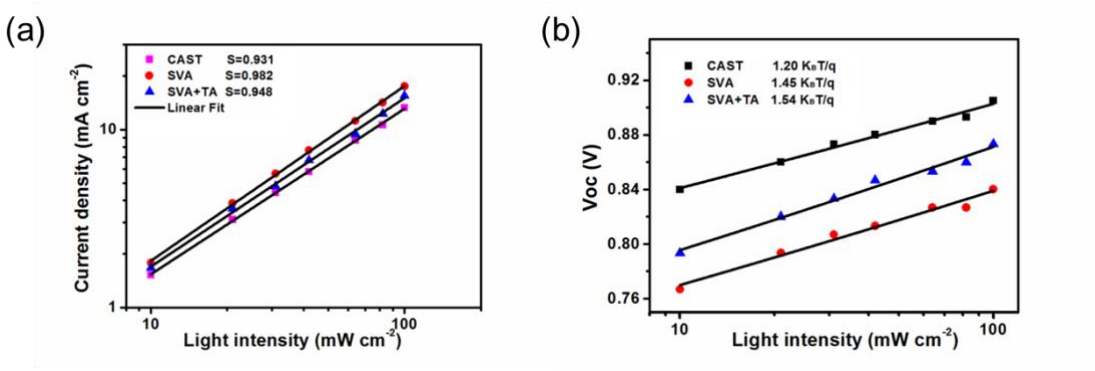

Figure 3. Dependence of J_{SC} (a) and V_{OC} (b) on light intensity for the ZnP2BT-RH based solar cells under three processing conditions.

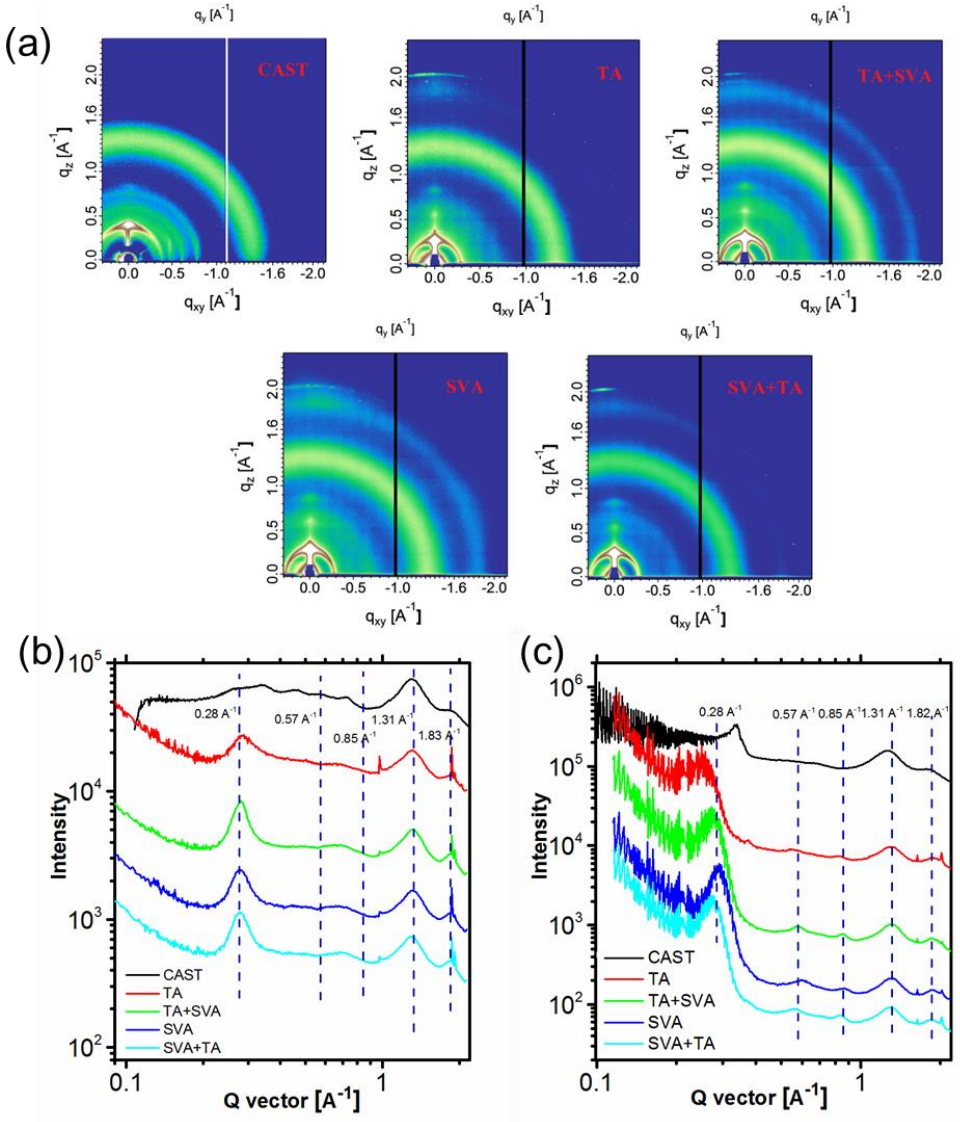

Figure 4. Grazing incidence X-ray diffraction (GIXD) pattern (a), in plane (b) and out of plane (c) line-cut profiles of BHJ thin films.

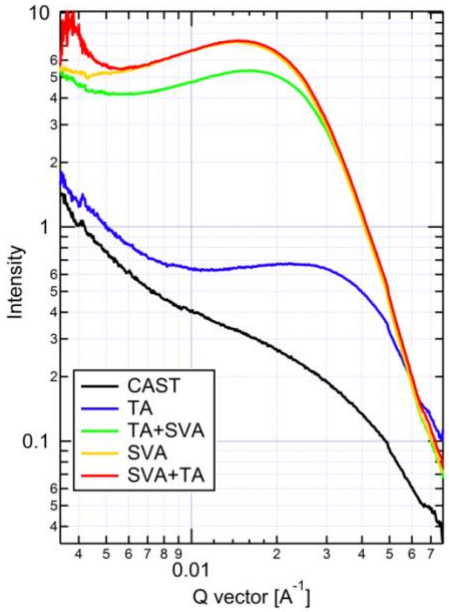

Figure 5. Resonant soft X-ray scattering (RSoXS) of BHJ thin films.

Table 1. The optical and electrochemical data of ZnP2BT-RH

λ_{max}/nm (solution)	λ_{max}/nm (film)	λ_{onset}/nm (film)	E_{ox} [V]	E_{HOMO}[a] [eV]	E_{LUMO}[b] [eV]	$E_{g(opt)}$ [eV]
507, 761	535, 792	885	0.77	−5.17	−3.77	1.40

a E_{HOMO} = −e (Eox +4.4) V; b E_{LUMO} = E_{HOMO}+ $E_{g(opt)}$.

Table 2. The photovoltaic parameters of ZnP2BT-RH-based solar cells under different process conditions.

Conditions	J_{SC} (mA cm^{-2})	V_{OC} (V)	*FF* (%)	PCE(%)
CAST	13.31±0.21	0.91±0.004	42.34±0.65	5.13±0.23[b] (5.23)[a]
TA	14.15±0.33	0.91±0.005	42.85±0.63	5.52±0.28[b] (5.68)[a]
TA+SVA	16.49±0.24	0.84±0.005	63.87±0.47	8.85±0.23[b] (9.00)[a]
SVA	17.49±0.24	0.84±0.005	66.79±0.55	9.81±0.24[b] (10.02)[a]
SVA+TA	15.79±0.31	0.86±0.010	55.97±0.66	7.60±0.37[b] (7.83)[a]

a The best PCE; b average PCE of 20 devices.

A novel dimeric porphyrin small molecule ZnP2BT-RH has been developed for OSC, and SVA treatment can induce obvious π–π stacking, suitable phase separation and improved phase purity. After optimizing the processing conditions, the devices exhibit a high power conversion efficiency up to 10% with a low energy loss (E_{loss}) of only 0.56 eV.

Keyword: dimeric porphyrin, organic solar cells, small photo energy loss, solvent vapor annealing

Liangang Xiao, Tianqi Lai, Xiang Liu, Feng Liu, Thomas P. Russell, Yi Liu*, Fei Huang*, Xiaobin Peng* and Yong Cao

A Low-Bandgap Dimeric Porphyrin Molecule for 10% Efficiency Solar Cells with Small Photon Energy Loss

ToC figure ((Please choose one size: 55 mm broad × 50 mm high **or** 110 mm broad × 20 mm high. Please do not use any other dimensions))

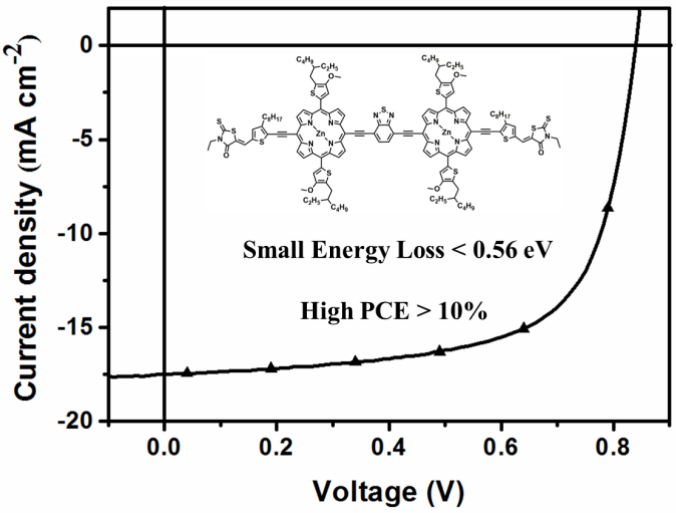

Supporting Information

A Low-Bandgap Dimeric Porphyrin Molecule for 10% Efficiency Solar Cells with Small Photon Energy Loss

Liangang Xiao, Tianqi Lai, Xiang Liu, Feng Liu, Thomas P. Russell, Yi Liu, Fei Huang*, Xiaobin Peng* and Yong Cao*

Experiment Details:

Materials: All reagents were purchased from commercial sources (Aldrich, Acros, Energy chemical or Suna Tech Inc.) and used as received. Tetrahydrofuran (THF) triethylamine (Et_3N) and toluene were dried over Na/benzophenoneketyl and freshly distilled prior to use.

Device Fabrication: The solution-processed BHJ solar cells were fabricated with a conventional device structure of Indium tin oxide (ITO)/PEDOT:PSS/ZnP2BT-RH:$PC_{71}BM$/PNDIT-F3N-Br/Al, and the fabrication details are as follows: ITO coated glass substrates were cleaned prior to device fabrication by sonication in acetone, detergent, distilled water, and isopropyl alcohol. After treated with an oxygen plasma for 4 min, 40 nm thick poly(styrene sulfonate)-doped poly(ethylene-dioxythiophene) (PEDOT:PSS) (Bayer Baytron 4083) layer was spin-casted on the ITO-coated glass substrates at 3000 rpm for 30 s, the substrates were subsequently dried at 150 ℃ for 10 min in air and then transferred to a N_2-glovebox. The active layers were prepared from ZnP2BT-RH:$PC_{71}BM$ in mixed solvent of chlorobenzene/pyridine (100:1 v/v) with an overall concentration of 30 mg/ml. The weight ratio of ZnP2BT-RH to $PC_{71}BM$ is varied from 1:1 to 1:2.5. For thermal annealing treatment, the active layer was annealed at different temperature for 5 mins. The optimal thermal annealing temperature is 135 ℃. For solvent vapor annealing treatment, the active layer was put in the petri dish containing 1 milliliter chloroform for different time. The optimal solvent vapor annealing time is 240 seconds. The thicknesses of active layers measured by a profilometer were to be about 110nm. The ultra-thin conjugated poly[(9,9-bis(3'-((N,N-dimethyl)-N-ethylammonium)propyl)-2,7-fluorene)-alt-5,5'-bis(2,2'-thiophene)-2,6-naphthalene-1,4,5,8-tetracaboxylic-N,N'-di(2-ethylhexyl)imide]dibromide (PNDIT-F3N-Br) layer was deposited by spin casting from a 0.03% (w/v) solution in methanol (from 2000 rpm for 30 s). Finally, Al (~80 nm) was evaporated with a shadow mask as the top electrode. The effective area was measured to be 0.16 cm_2.

Measurements and Instruments: $_1$H NMR spectra were recorded using a Bruker Ultrashield 500 Plus NMR spectrometer. High-resolution matrix-assisted laser desorption/ionization time-off light (MALDI-TOF) mass spectra were obtained with a Bruker Autoflex MALDITOF mass spectrometer. UV-vis spectra of dilute solutions of samples in dichloromethane (THF) were recorded at room temperature (ca. 25°C) using a Shimadzu UV-3600 spectrophotometer. Solid films for UV-vis spectroscopic analysis were obtained by spin-coating the solutions onto a quartz substrate. Cyclic voltammetry (CV) was carried out on a CHI660A electrochemical workstation with platinum electrodes at a rate of 50 mV s^{-1} against an Ag/AgCl reference electrode with nitrogen-staturated solution of 0.1 M tetrabutylammonium hexafluorophosphate (Bu_4NPF_6) in acetonitrile (CH_3CN).

PCEs were determined from J-V characteristics measured by a Keithley 2400 source-measurement unit under AM 1.5G spectrum from a solar simulator (Oriel model 91192). Masks made from laser beam cutting technology with a well-defined area of 0.16 cm^2 were attached to define the effective area for accurate measurement. Solar simulator illumination intensity was determined using a monocrystal silicon reference cell (Hamamatsu S1133, with KG-5 visible color filter) calibrated by the National Renewable Energy Laboratory (NREL). The tapping mode atomic force microscopy (AFM) measurements of the blends' surface morphology were conducted on a NanoScope NS3A system (Digital Instrument). External quantum efficiency (EQE) values of the encapsulated devices were measured by using an integrated system (Enlitech, Taiwan, China) and a lock-in amplifier with a current preamplifier under short-circuit conditions. The devices were illuminated by monochromatic light from a 75 W xenon lamp. The light intensity was determined by using a calibrated silicon photodiode.

Grazing incidence X-ray diffraction (GIXD) characterization of the thin films was performed at beamline 7.3.3 Lawrence Berkeley National Lab. The scattering signal was

recorded on a 2-D detector (Pilatus 1M) with a pixel size of 172 μm. The X-ray energy is 10 keV. The samples were ~15 mm long in the direction of the beam path, and the detector was located at a distance of 300 mm from the sample center (distance calibrated using a silver behenet standard). The incidence angle of 0.16° was chosen which gave the optimized signal-to-background ratio. Thin film samples were prepared on PEDOT:PSS covered silicon wafers to match the device conditions. The data was processed and analyzed using Nika software package. RSoXS was performed at beamline 11.0.1.2 Lawrence Berkeley National Lab. A 284.2 eV beamline energy at $PC_{61}BM$ k-edge was chosen to enhance the contrast. Thin films of device thickness was flowed and transferred onto Si_3N_4 substrates, which were then mounted onto sample plate.

Capacitance-voltage characteristics: We measured the relative dielectric constants of all the materials with a device structure of ITO/PEDOT:PSS/small molecule or polymer films/Al. Capacitance-voltage (C-V) measurements were performed using a HP 4192A LCR meter by sweeping the voltage from -10V to +10V at room temperature, with ramping rate of 0.5 V/s and 30 mV of oscillator levels. Figure S7 shows corresponding dielectric constants of small molecule or polymer films with respect to frequency (10^3 to 5×10^5 Hz). The dielectric constant was calculated from the following equation:

$$\varepsilon_r = \frac{Cd}{\varepsilon_0 A}$$

ε_r is the relative dielectric constant of the material, ε_0 is the dielectric constant of free space, d is the thickness of the active films, A is the capacitor area (0.16 cm^2), C is the capacitance of the device.

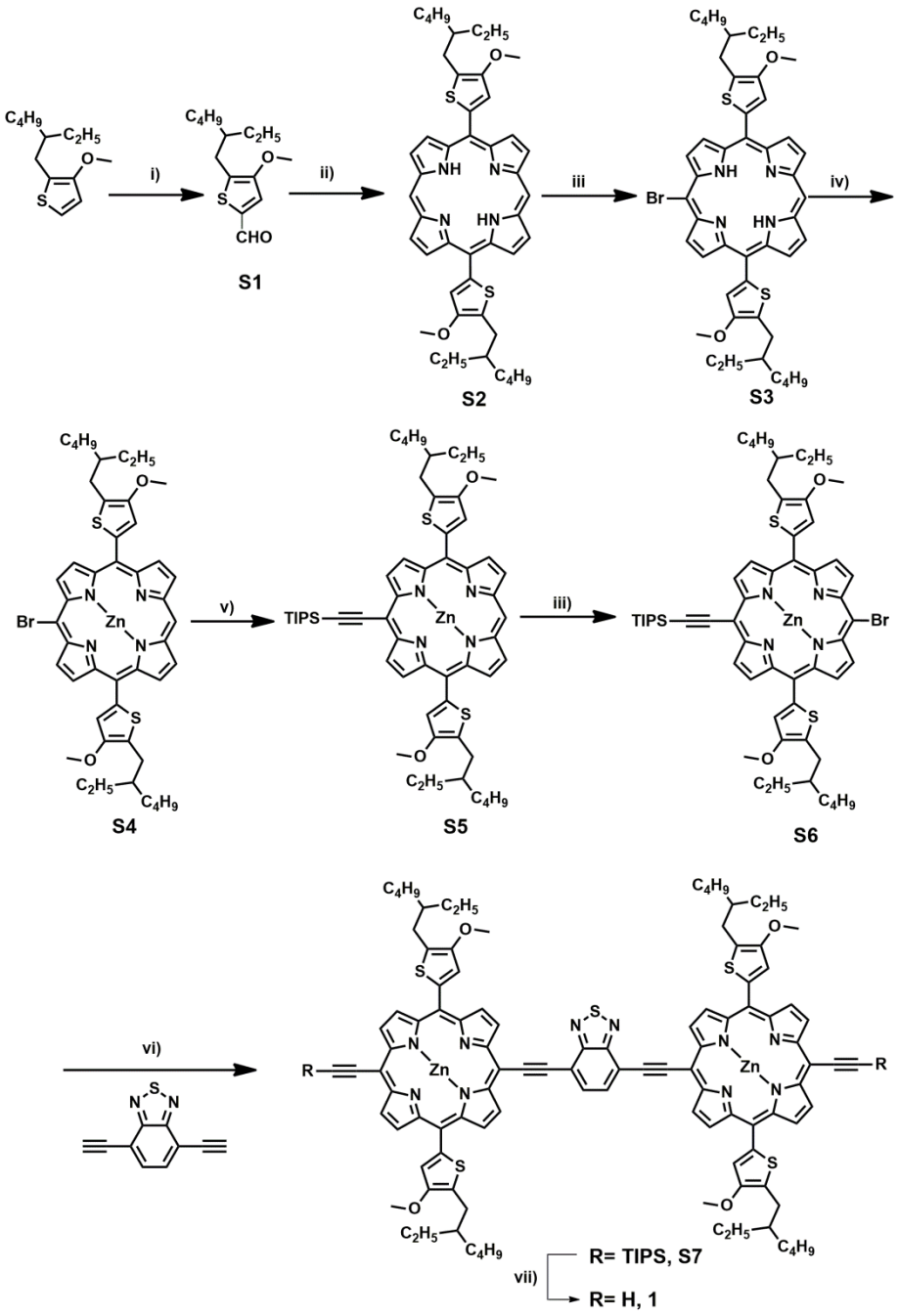

Scheme S1. Synthesis routes for porphyrin unit (1): (i)DMF, $POCl_3$; (ii)DCM, TFA, DDQ; (iii) NBS, $CHCl_3$; (iv) Zn(OAc)2, $CHCl_3$/MeOH; (v) TIPSA, $Pd(PPh_3)_2Cl_2$, CuI, THF/Et_3N; (vi) $Pd(PPh_3)_4$, CuI, THF/Et_3N; (vii)TBAF, THF.

We synthesized 2-(2-ethylhexyl)-3-methoxythiophene,[1] 5-bromo-10,20-bis[5-(2-ethylhexyl)-4-methoxythiophene-2-yl]-porphyrin(2)[2] and 4,7-Diethynyl-benzo[c][1,2,5]thiadiazole[3] according to literature procedures.

5-(2-ethylhexyl)-4-methoxythiophene)-2-carbaldehyde (S1):

To a stirred solution of (2-(2-ethylhexyl)-3-methoxythiophene) (13.6 g, 59.4 mmol) in DMF, $POCl_3$ (13.0 g, 180.0 mmol) was added drop-wise at 0 ^oC, stirring was warmed neutralized by NaOH to neutrality. After extraction with $CHCl_3$, the organic phase was dried over $MgSO_4$. The crude product was purified by column chromatography on silica gel using ethyl acetate/petroleum ether (v/v = 1/4) as the eluent to give 9.49g pure product in 66.8 yield. Yellow oil; ^1H NMR (500 MHz, CDCl3) δ (ppm): 9.72 (s, 1H), 7.46 (s, 1H), 3.87 (s, 3H), 2.69 (d, 2H), 1.56-1.67(m, 1H), 1.21-1.37 (m, 8H), 0.84-0.92 (t, 6H).

5,15-Bis-(5-(2-ethylhexyl)-4-methoxythiophene)-2-yl)-porphyrin (S2):

A solution of 5-(2-(2-ethylhexyl)-3-methoxythiophene)-2-carbaldehyde (4.74g, 18.66 mmol) and dipyrromethane (2.72g, 18.66 mmol) in CH_2Cl_2 (1.5L) was purged with nitrogen for 30 min, and then trifluoroacetic acid (TFA) (0.22 mL) was added. The mixture was stirred for 12h at room temperature, and then 2,3-dichloro-5,6-dicyano-1,4-benzoquinone (DDQ) (6.90g) was added. After the mixture was stirred at room temperature for an additional 1h, the reaction was quenched by triethylamine (5 mL). Then the solvent was removed, and the residue was purified by flash column chromatography on silica gel using dichloromethane as the eluent. Recrystallization from CH_2Cl_2/methanol gave S**2** as a dark red solid (2.26g, 32%). ^1H NMR(500 MHz, CDCl3) δ (ppm): 10.27 (s, 2H), 9.38 (s, 8H), 7.72 (s, 2H), 4.10 (s, 6H), 3.20 (d, 4H), 1.83-1.93(m, 2H), 1.40-1.69 (m, 16H), 0.97-1.17 (m, 12H), -2.97 (s, 2H).

5-bromo-10,20-bis[5-(2-ethylhexyl)-4-methoxythiophene-2-yl]-porphyrin (S3):

Porphyrin S**2** (1.26 g, 1.66mmol) were dissolved in 600 mL chloroform and pyridine (5 mL) and then cooled to 0 ^oC. To the cold solution, N-bromosuccinimide (295 mg, 1.66 mmol) was added and the mixture was stirred at 0 °C for 30 min. Then the reaction was quenched by acetone, and the mixture was washed with water and dried over anhydrous Na_2SO_4. After the

solvent was removed, the residue was purified by flash column chromatography on silica gel using petroleum ether/dichloromethane (2:1) as the eluent. Recrystallization from CH_2Cl_2/methanol gave S**3** as a purple solid (0.90 g, 65%). ^{1}H NMR (500 MHz, $CDCl_3$) δ 10.11 (s, 1H), 9.73 (d, *J* = 4.8 Hz, 2H), 9.30-9.19 (m, 6H), 7.68 (s, 2H), 4.09 (s, 6H), 3.00 (dd, *J* = 7.0, 1.0 Hz, 4H), 1.92-1.78 (m, 2H), 1.68-1.37 (m, 6H), 1.04 (dt, *J* = 35.1, 7.2 Hz, 12H), -2.92 (s, 2H). ^{13}C NMR (126 MHz, $CDCl_3$) δ 153.1, 136.3, 132.6, 131.7, 125.5, 124.3, 112.9, 106.1, 104.4, 77.2, 59.4, 41.2, 32.8, 29.9, 29.1, 26.1, 23.2, 14.3, 11.1.

5-bromo-10,20-bis[5-(2-ethylhexyl)-4-methoxythiophene-2-yl]-porphinato)zinc (II) (S4):

Compound S**3** (904 mg, 1.08 mmol) was dissolved in a mixture of 200 ml chloroform. A solution of zinc acetate dihydrate (1.01 g, 5.4 mmol) in methanol (20 ml) was added, and the reaction mixture was stirred at 60 ^{o}C for 4 h. After routine procedures, the solvent was evaporated, and the residue was chromatographed on silicagel using $CHCl_3$ as the eluent to give S**4** as a purple solid (953 mg, 98%).^{1}H NMR (500 MHz, $CDCl_3$) δ 9.97 (s, 1H), δ 9.84 (d, *J* = 4.6 Hz, 2H), 9.31 (d, *J* = 4.6 Hz, 2H), 9.26-9.18 (m, 4H), 7.52 (s, 2H), 3.90 (s, 6H), 2.87 (d, *J* = 6.9 Hz, 4H), 1.73-1.85 (m, 2H), 1.64-1.36 (m, 16H), 1.01 (dt, *J* = 23.4, 7.3 Hz, 12H). ^{13}C NMR (126 MHz, $CDCl_3$) δ 147.8, 147.7, 146.3, 145.8, 144.8, 132.6, 128.0, 127.6, 127.2, 126.4, 119.9, 119.01, 109.1, 104.5, 103.0, 54.6, 36.4, 28.0, 24.90, 24.3, 21.3, 18.4, 14.4, 9.5, 7.2, 6.3.

5-((Triisopropylsilyl)ethynyl)-10,20-bis[5-(2-ethylhexyl)-4-methoxythiophene-2yl]-porphinato)zinc (II) (S5):

The mono-bromo compound S**4** (920 mg, 1.02 mmol) was dissolved in THF (40 mL), and then triethylamine (20 mL) was added. The mixture was purged with argon for 30 min. Then $Pd(PPh_3)_2Cl_2$ (70 mg, 0.10 mmol), CuI (19 mg, 0.10 mmol), and (triisopropylsilyl)acetylene (926 mg, 5.1 mmol) were added. After the mixture was stirred at

room temperature for 24 h under Ar, the reaction was quenched with brine. Then the mixture was extracted with dichloromethane, dried with anhydrous Na_2SO_4 and concentrated. Finally, the residue was purified on column chromatography to afford S**5** as a purple solid (940 mg, 92% yield). ^{1}H NMR (500 MHz, $CDCl_3$) δ9.98 (s, 1H), 9.84 (d, *J* = 4.6 Hz, 2H), 9.31 (d, *J* = 4.6 Hz, 2H), 9.26-9.18 (m, 4H), 7.52 (s, 2H), 3.90 (s, 6H), 2.87 (d, *J* = 6.9 Hz, 4H), 1.72-1.84 (m, 2H), 1.64-1.36 (m, 37H), 1.01 (dt, *J* = 23.4, 7.3 Hz, 12H). ^{13}C NMR (126 MHz, $CDCl_3$) δ 147.8, 147.7, 146.3, 145.8, 144.8, 132.6, 128.1, 127.6, 127.2, 126.4, 119.9, 119.1, 109.0, 104.5, 103.0, 96.5, 93.4, 54.6, 36.4, 28.0, 25.4, 24.9, 24.3, 21.3, 18.4, 14.4, 9.5, 7.2, 6.3.

5-bromo-15-((triisopropylsilyl)ethynyl)-10,20-bis[5-(2-ethylhexyl)-4-methoxythiophene-2yl]-porphinato)zinc (II) (S**6**):

Compound S**5** (900 mg, 0.89 mmol) was dissolved in 200 ml of chloroform and 2 ml of pyridine. After the reaction mixture was cooled to 0 ˚C, N-bromosuccinimide (240 mg, 1.35 mmol) was added to the reaction mixture and stirred for 30 min. Then the reaction mixture was washed with water, dried over Na_2SO_4, and concentrated. And the residue was purified first by column chromatography on silica gel to give S**6** as a dark green solid (689 mg, 71% yield). ^{1}H NMR (500 MHz, $CDCl_3$) δ 9.73 (d, *J* = 4.6 Hz, 2H), 9.62 (d, *J* = 4.6 Hz, 2H), 9.18 (d, *J* = 4.6 Hz, 2H), 9.14 (d, *J* = 4.7 Hz, 2H), 7.43 (s, 2H), 3.82 (s, 6H), 2.81 (d, *J* = 6.8 Hz, 4H), 1.79-1.68 (m, 2H), 1.61-1.35 (m, 37H), 1.00 (dt, *J* = 16.7, 7.3 Hz, 12H). ^{13}C NMR (126 MHz, $CDCl_3$) δ 153.3, 152.4, 151.5, 150.9, 149.5, 143.0, 137.2, 133.2, 133.0, 132.9, 131.4, 124.8, 123.9, 114.7, 109.2, 106.7, 101.4, 98.4, 77.2, 65.4, 59.3, 41.1, 32.7, 29.6, 29.0, 26.0, 23.2, 19.1, 19.0, 14.3, 11.9, 11.0.

4,7-Bis[(15-[(triisopropylsilyl)ethynyl]-10,20-bis[5-(2-ethylhexyl)-4-methoxythiophene-2yl]-porphinato)zinc(II)-5-ylethyny]benzo[*c*][1,2,5]thiadiazole (S7):

Compound **S6** (675mg, 0.62mmol) and 4,7-Diethynyl-benzo[*c*][1,2,5]thiadiazole (50 mg, 0.27 mmol) were dissolved in THF (40 mL) with triethylamine (20 mL). Then Pd_2dba_3 (24 mg, 0.03 mmol) and $P(PPh_3)_4$ (72 mg, 0.06 mmol) were added. The mixture was stirred at 60 ^oC for 48 h under argon protection, then the reaction mixture was poured into water and extracted with $CHCl_3$ and washed with brine, dried over Na_2SO_4, and evaporated. The residue was chromatographed on silica gel to isolate the desired product, which was then further purified via GPC to afford compound S**7** (450mg, 76% yield). ^1H NMR (500 MHz, $CDCl_3$) δ 10.07 (d, *J* = 4.5 Hz, 4H), 9.67 (d, *J* = 4.5 Hz, 4H), 9.28 (d, *J* = 4.5 Hz, 4H), 9.16 (d, *J* = 4.4 Hz, 4H), 8.27 (s, 2H), 7.65 (s, 4H), 4.06 (s, 12H), 2.98 (d, *J* = 6.9 Hz, 8H), 1.89-1.78 (m, 4H), 1.68-1.35 (m, 74H), 1.02 (dt, *J* = 31.3, 7.3 Hz, 24H). ^{13}C NMR (126 MHz, $CDCl_3$) δ 155.4, 152.8, 152.5, 151.1, 150.9, 137.9, 132.9, 132.4, 131.4, 131.1, 124.4, 123.7, 117.6, 115.2, 109.8, 102.7, 102.4, 100.6, 98.11, 93.6, 77.3, 59.4, 41.2, 32.8, 29.8, 29.1, 26.1, 23.2, 19.1, 14.3, 11.9, 11.1.

4,7-Bis[(15-ethynyl-10,20-bis[5-(2-ethylhexyl)-4-methoxythiophene-2yl]-porphinato)zinc(II)-5-ylethyny]benzo[*c*][1,2,5]thiadiazole (1):

TBAF (1 M in THF, 0.46 mmol) was added to compound S**7** (436mg, 0.20 mmol) in 10 mL of THF at room temperature. After the mixture was stirred for 15 min, the mixture was poured into water, extracted with $CHCl_3$ and dried over Na_2SO_4, it was allowed to pass through a short silica gel column and to afford crude **8**, which were used directly for the next reaction without further purification.

ZnP2BT-RH: Compound **1** (187mg, 0.10 mmol) was dissolved in THF (20 mL) and triethylamine (10 mL) with compound **2** (0.30 mmol). Then $Pd(PPh_3)_4$ (12 mg, 0.01mmol) and CuI (2 mg, 0.01mmol) were added. After the mixture was stirred at 60 ^oC for 48 h under argon, the reaction was quenched with saturated brine. After the mixture was extracted with

chloroform, dried with anhydrous Na_2SO_4 and concentrated. The residue was column chromatographed on silica gel using CH_2Cl_2 as eluent to give a black solid of **ZnP2BT-RH**. (170 mg, 65% yield).

ZnP2BT-RH: ^{1}HNMR (500 MHz, $CDCl_3$) δ/ppm (ppm): ^{1}HNMR (500 MHz, $CDCl_3$) δ/ppm (ppm): 10.66-9.60 (m, 16H), 8.58-7.73 (m, 12H), 7.58 (s, 4H), 6.45(s, 2H), 4.36 (s, 12H), 3.64-3.27 (m, 8H), 2.45-2.15 (m, 4H), 2.15-1.04 (m, 86H), 0.91 (s, 6H). MALDI−TOF Mass (m/z): calculated for $C_{142}H_{150}N_{12}O_6S_{11}Zn_2$: 2601.73; found: 2602.25; UV-vis (THF), λ_{max}=508 nm.

List of Figures and tables

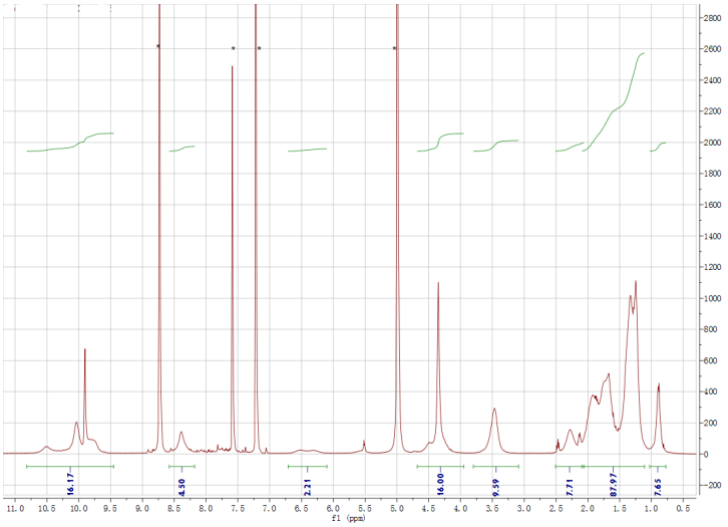

Figure S1. The ^{1}H NMR(500 MHz) spectrum of **ZnP2BT-RH** in Pyridine-d_5.

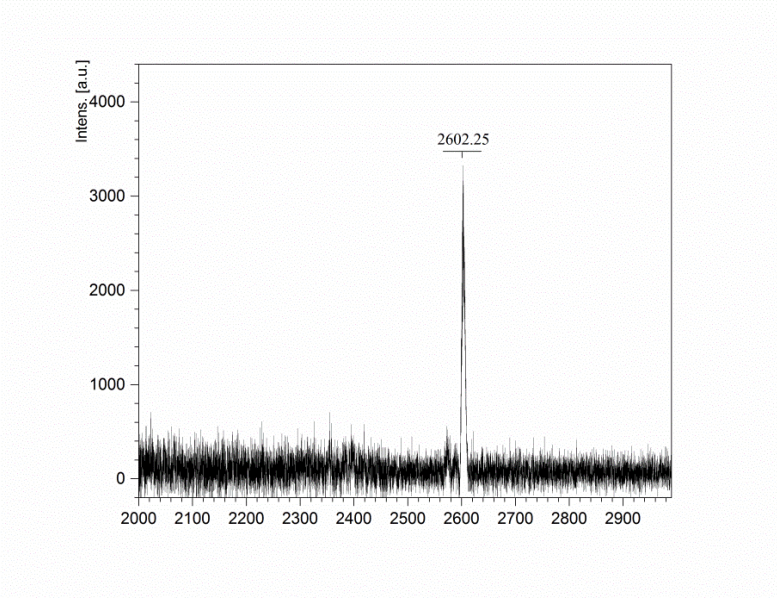

Figure S2. The high-resolution matrix-assisted laser desorption/ionization time-off light (MALDI-TOF) mass spectra of **ZnP2BT-RH**.

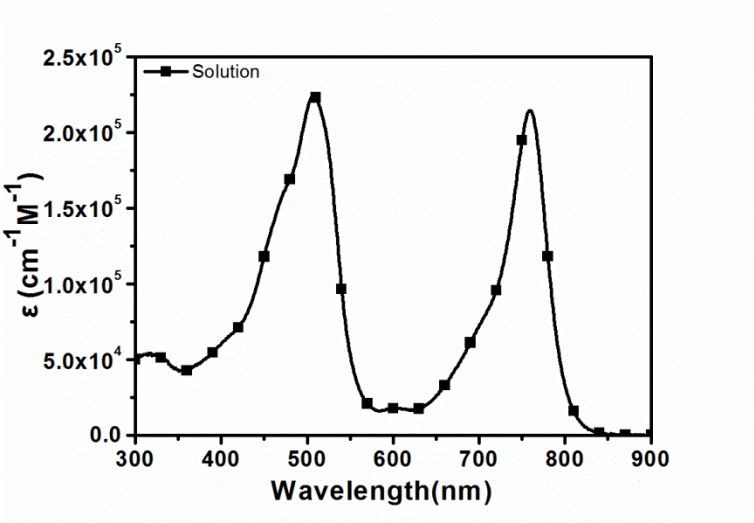

Figure S3. UV–vis–NIR absorption spectrum of **ZnP2BT-RH** in solution

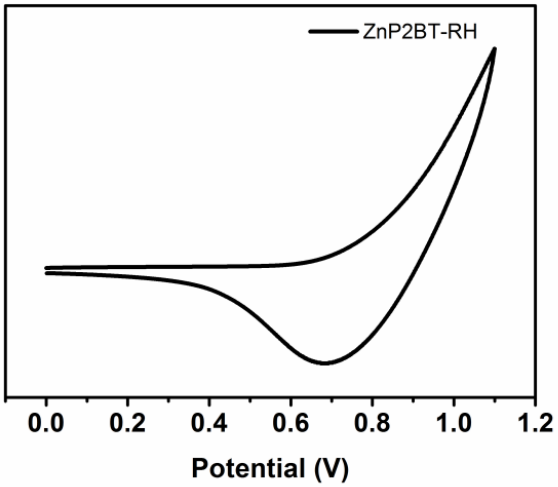

Figure S4. Cyclic voltammograms of **ZnP2BT-RH** film in acetonitrile containing 0.10 M tetrabutylammonium hexafluorophosphate (Bu_4NPF_6) as the supporting electrolyte and an Ag/AgCl electrode as the reference electrode speed of 50 mV s^{-1}.

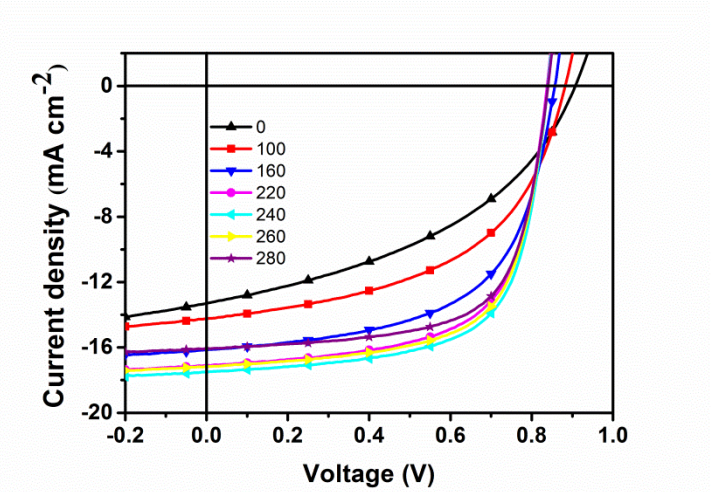

Figure S5. J-V curves of ZnP2BT-RH:$PC_{71}BM$ (w/w= 1:1.5) based solar cells under different SVA time.

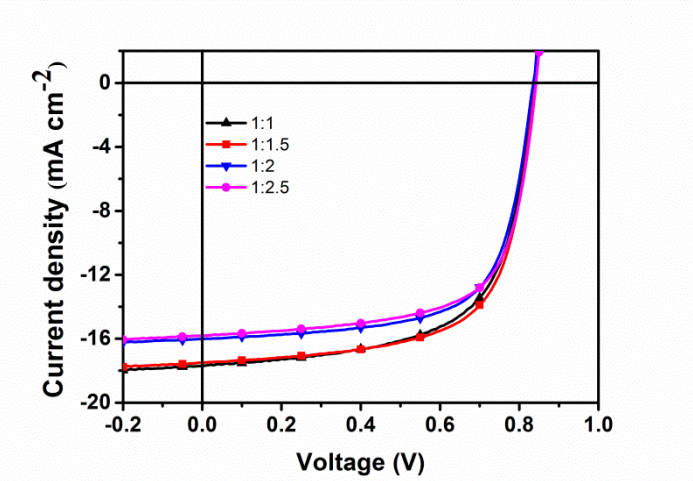

Figure S6. J-V curves of ZnP2BT-RH-based solar cells with various ZnP2BT-RH/$PC_{71}BM$ ratios under optimal SVA processing condition.

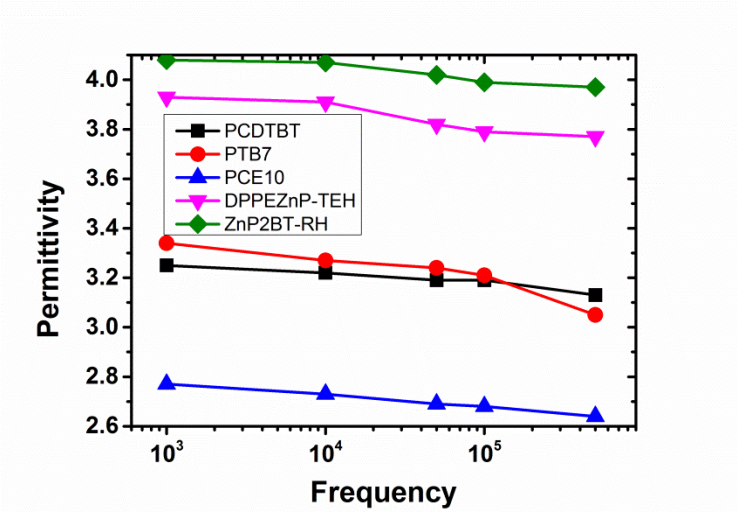

Figure S7. Relative dielectric constant (εr) of small molecule or polymer films with respect to frequency from 10_3 to $5\times10_5$ HZ.

Figure S8. Dark J-V curves of ZnP2BT-RH-based solar cells under different process conditions.

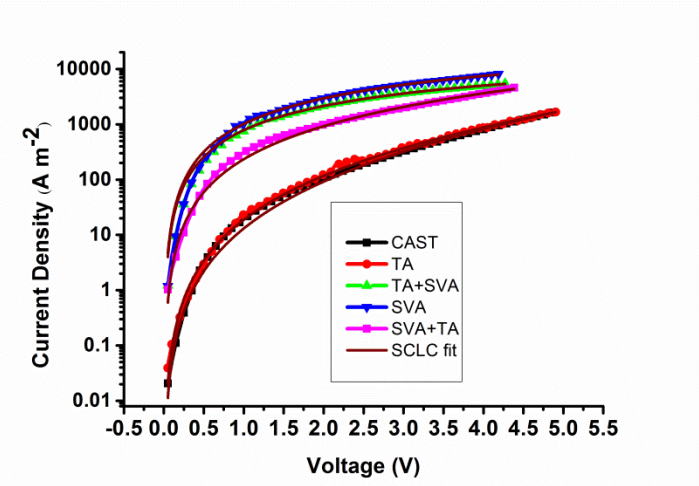

Figure S9. J-V characteristics in the dark under different processing conditions based on device structures of ITO/PEDOT:PSS/ZnP2BT-RH:$PC_{71}BM$/MoO_3/Ag.

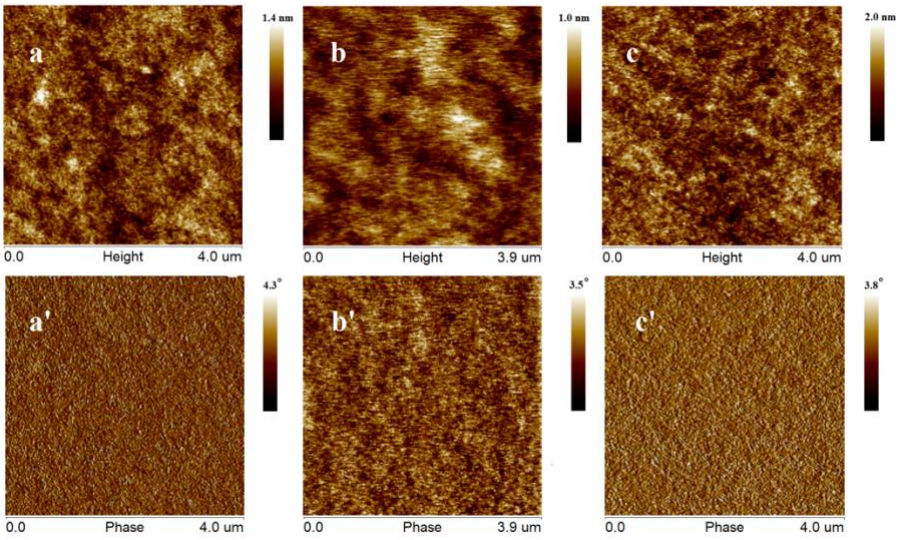

Figure S10. AFM height images (a-c) and phase images (a'-c') of blend films based ZnP2BT-RH:$PC_{71}BM$. a) cast, b) SVA and c) TA+SVA.

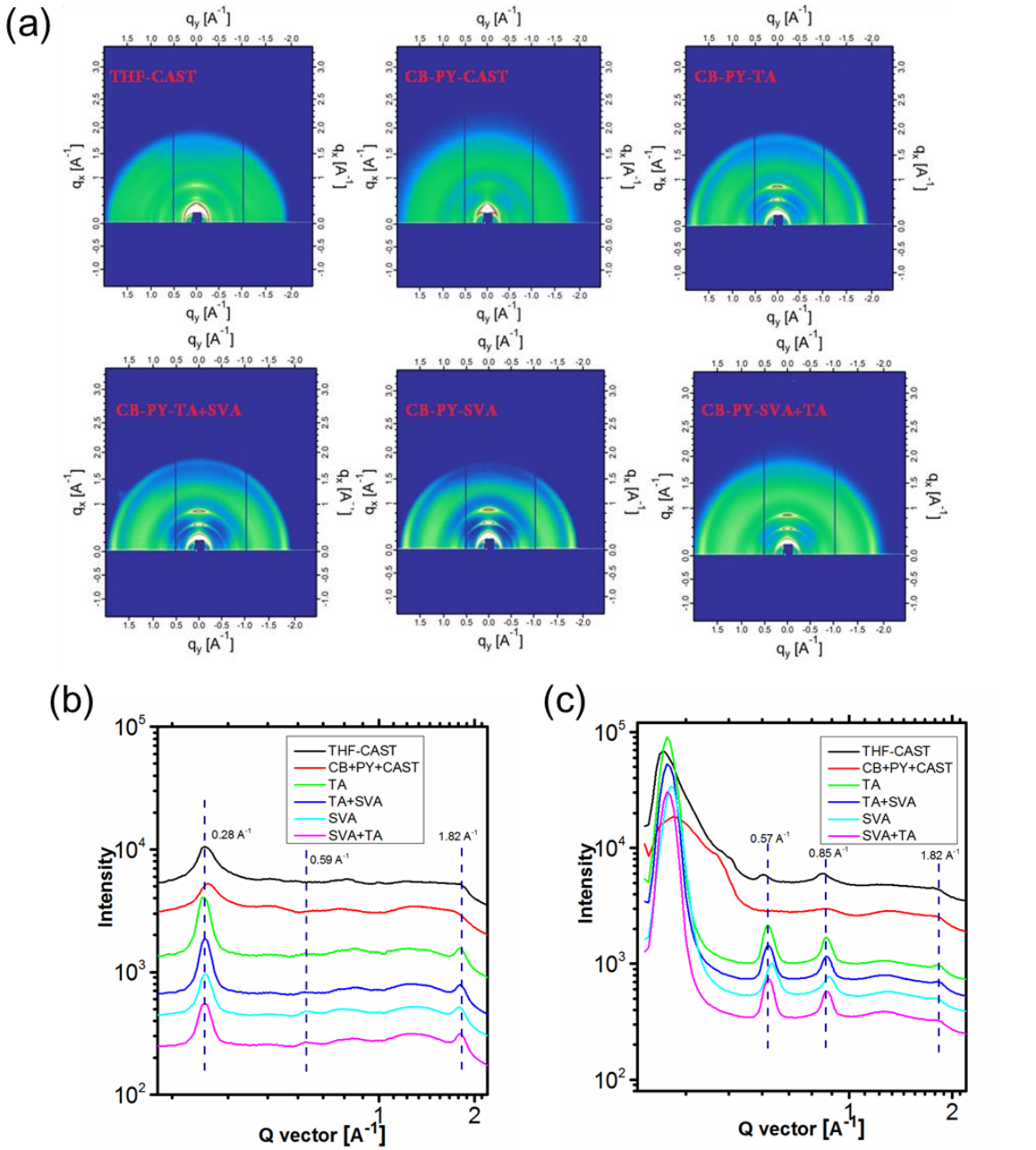

Figure S11. Grazing incidence X-ray diffraction (GIXD) pattern (a), in plane (b) and out of plane (c) line-cut profiles of pure films.

Table S1. The photovoltaic parameters of ZnP2BT-RH:$PC_{71}BM$ (w/w= 1:1.5) based solar cells under different thermal annealing temperature.

temperature	J_{SC} (mA cm^{-2})	V_{OC} (V)	*FF* (%)	*PCE*(%)
RT	13.31±0.21	0.91±0.004	42.34±0.65	5.13±0.23(5.23)
120	13.78±0.22	0.91±0.005	42.32±0.55	5.31±0.19(5.23)
135	14.15±0.33	0.91±0.005	42.85±0.63	5.52±0.28(5.68)

150	13.45±0.32	0.90±0.005	40.75±0.53	4.93±0.20(5.05)

Table S2. The photovoltaic parameters of ZnP2BT-RH:$PC_{71}BM$ (w/w= 1:1.5) based solar cells under different SVA time.

SVA time (Seconds)	J_{SC} (mA cm^{-2})	V_{OC} (V)	*FF* (%)	*PCE*(%)
0	13.31±0.21	0.91±0.004	42.34±0.65	5.13±0.23(5.23)
100	14.22±0.22	0.88±0.004	51.72±0.55	6.48±0.21(6.67)
160	16.14±0.22	0.86±0.005	59.04±0.45	8.20±0.18(8.34)
220	17.08±0.23	0.84±0.005	64.89±0.56	9.31±0.25(9.51)
240	17.49±0.24	0.84±0.005	66.79±0.55	9.81±0.24(10.02)
260	17.16±0.24	0.84±0.005	66.45±0.49	9.58±0.23(9.70)
280	16.05±0.25	0.84±0.005	67.17±0.45	9.06±0.23(9.22)

Table S3. The photovoltaic parameters of ZnP2BT-RH-based solar cells with various ZnP2BT-RH:$PC_{71}BM$ ratio under optimal SVA processing condition.

weight ratio	J_{SC} (mA cm^{-2})	V_{OC} (V)	*FF* (%)	*PCE*(%)
1:1	17.82±0.24	0.84±0.005	63.53±0.55	9.51±0.18(9.61)
1:1.5	17.49±0.24	0.84±0.005	66.79±0.55	9.81±0.24(10.02)
1:2	16.02±0.22	0.84±0.005	67.81±0.44	9.12±0.19(9.24)
1:2.5	15.82±0.20	0.84±0.005	67.47±0.53	8.97±0.21(9.12)

Table S4. Summary of some high performance organic solar cells and with low energy loss.

Solar cells	PCEs	Material types		Bandgap (eV)	E_{loss} (eV)	Ref
		Molecules	Polymers			
DR3TSBDT:$PC_{71}BM$	9.95%	✓		1.74	0.83	[4]
BDTSTNTTR:$PC_{71}BM$	11.53%	✓		1.50	0.67	[5]
BIT6F:$PC_{71}BM$	9.09%	✓		1.79	0.90	[6]
BTID-2F:$PC_{71}BM$	11.30%	✓		1.68	0.73	[7]
PTB7-Th: F8IC	10.90%		✓	1.27	0.64	[8]
PNOz4T:$PC_{71}BM$	8.90%		✓	1.52	0.56	[9]

J61:ITIC	9.53%		✓	1.57	0.68	[10]
P3TEA:SF-PDI2	9.50%		✓	1.72	0.61	[11]
PffBX-T3:ITIC-Th	7.40%		✓	1.60	0.53	[12]
PBDTT-SF-TT: $PC_{71}BM$	9.07%		✓	1.59	0.59	[13]
PffBT4T-2DT:IDTBR	10.00%		✓	1.62	0.55	[14]
ZnP2BT-RH:PC71BM	10.02%	✓		1.40	0.56	This work

Table S5. Hole mobility of ZnP2BT-RH:$PC_{71}BM$ based devices.

conditions	*CAST*	*TA*	*TA+SVA*	*SVA*	*SVA+TA*
Value ($cm^2\ V^{-1}\ s^{-1}$)	1.21×10^{-5}	1.43×10^{-5}	3.40×10^{-4}	4.94×10^{-4}	1.08×10^{-4}

references

[1] W. Huag, M. L. Li, L. Z. Zhang, T. B. Yang, Z. Zhang, H. Zeng, X. Zhang, L. Dang, Y. Y. Liang, *Chem. Mater.* **2016**, *28*, 5887-5895.

[2] T. Lai, X. Chen, L. Xiao, L. Zhang, T. Liang, X. Peng, Y. Cao, *Chem. Commun.* **2017**, *53*, 5113-5116.

[3] J. J. Bryant, B. D. Lindner, U. H. F. Bunz, *J. Org. Chem.* **2013**, *78*, 1038-1044.

[4] B. Kan, Q. Zhang, M. M. Li, X. J. Wan, W. Ni, G. K. Long, Y. C. Wang, X. Yang, H. R. Feng, Y. S. Chen, *J Am Chem Soc* **2014**, *136*, 15529-15532.

[5] J. H. Wan, X. P. Xu, G. J. Zhang, Y. Li, K. Feng, Q. Peng, *Energ Environ Sci* **2017**, *10*, 1739-1745.

[6] J. L. Wang, K. K. Liu, J. Yan, Z. Wu, F. Liu, F. Xiao, Z. F. Chang, H. B. Wu, Y. Cao, T. P. Russell, *J Am Chem Soc* **2016**, *138*, 7687-7697.

[7] D. Deng, Y. J. Zhang, J. Q. Zhang, Z. Y. Wang, L. Y. Zhu, J. Fang, B. Z. Xia, Z. Wang, K. Lu, W. Ma, Z. X. Wei, *Nat Commun* **2016**, *7*, 13740-13748.

[8] P. Cheng, M. Y. Zhang, T. K. Lau, Y. Wu, B. Y. Jia, J. Y. Wang, C. Q. Yan, M. Qin, X.

H. Lu, X. W. Zhan, *Adv. Mater.* **2017**, *29*, 1605216-1605221.

[9] B. Kan, Q. Zhang, M. M. Li, X. J. Wan, W. Ni, G. K. Long, Y. C. Wang, X. Yang, H. R. Feng, Y. S. Chen, *J. Am. Chem. Soc.* **2014**, *136*, 15529-15532.

[10] K. Kawashima, Y. Tamai, H. Ohkita, I. Osaka, K. Takimiya, *Nat. Commun.* **2015**, *6*, 10085-10093.

[11] H. J. Bin, Z. G. Zhang, L. Gao, S. S. Chen, L. Zhong, L. W. Xue, C. Yang, Y. F. Li, *J. Am. Chem. Soc.* **2016**, *138*, 4657-4664.

[12] J. Liu, S. S. Chen, D. P. Qian, B. Gautam, G. F. Yang, J. B. Zhao, J. Bergqvist, F. L. Zhang, W. Ma, H. Ade, O. Inganas, K. Gundogdu, F. Gao, H. Yan, *Nat. Energy* **2016**, *1*, 16089-16095.

[13] J. Zhang, K. Jiang, G. Yang, T. Ma, J. Liu, Z. Li, J. Y. L. Lai, W. Ma, H. Yan, *Adv. Energy Mater.* **2017**, 1602119-1602126.

[14] Z. Du, X. Bao, Y. Li, D. Liu, J. Wang, C. Yang, R. Wimmer, L. W. Städe, R. Yang, D. Yu, *Adv. Energy Mater.*, 1701471-1701482.